



An evaluation of the Arabian Sea Mini Warm Pool's advancement during its mature phase using a coupled atmosphere–ocean numerical model

Sankar Prasad Lahiri¹, Kumar Ravi Prakash^{1,2}, and Vimlesh Pant¹

¹Centre for Atmospheric Sciences, Indian Institute of Technology, Delhi, India

²Applied Physics Laboratory, University of Washington, Seattle, WA, USA

Correspondence: Sankar Prasad Lahiri (sankarprasadlahiri2@gmail.com)

Received: 11 September 2024 – Discussion started: 24 September 2024

Revised: 3 March 2025 – Accepted: 2 April 2025 – Published: 8 July 2025

Abstract. A coupled atmosphere–ocean numerical model is used to examine the relative contributions of atmospheric and oceanic processes in developing the Arabian Sea Mini Warm Pool (MWP). The model simulations were performed for three independent years, 2013, 2016, and 2018, through April–June, and the results were compared against observations. The model-simulated sea surface temperature (SST) and sea surface salinity (SSS) bias were less than 1.75 °C and 1 psu, respectively; this bias was minimal in the MWP region. Moreover, the model simulated results effectively represented the presence of the MWP across the three different years. The mixed-layer heat budget analysis indicated that the net surface heat flux raised the mixed-layer temperature tendency of the MWP by a maximum of 0.1 °C d⁻¹ during its development phase. The vertical processes exerted a cooling impact on the temperature tendency throughout May and June with a maximum of −0.08 °C d⁻¹. Nonetheless, the decrease of net surface heat flux emerged as the dominant factor for the dissipation of the MWP. Further, four sensitivity numerical experiments were performed to investigate the comparative consequences of the ocean and atmosphere on the advancement of the MWP. The sensitivity experiments indicated that pre-April ocean conditions in years with a strong MWP resulted in a 136 % increase in MWP intensity in years when MWP SST was close to the climatology, which shows the primary role of oceanic preconditioning in determining MWP strength during strong-MWP years. Once the oceanic preconditions are met, the atmospheric conditions of weak-MWP years lead to an 82 % reduction in MWP intensity relative to normal years, highlighting the detrimental impact of

atmospheric forcing under such circumstances. Atmospheric conditions, particularly wind, are critical in influencing the spatial evolution and dissipation of the MWP in the south-eastern Arabian Sea (SEAS). A wind shadow zone, characterized by less production of turbulent kinetic energy that does not exist during weak-MWP years, facilitates the spatial expansion of the MWP in SEAS during moderate to strong-MWP years.

1 Introduction

The north Indian Ocean (NIO) associated ocean–atmosphere dynamics, including monsoons and cyclones, are well explored by researchers. One of the primary determinants in this interconnected process is the sea surface temperature (SST). During the pre-monsoon season, the southern region of the Arabian Sea experiences SST exceeding 28 °C, which is associated with the larger Indo-Pacific Warm Pool. However, the highest temperature is observed in the south-eastern Arabian Sea (SEAS) from late April to May, before the onset of the Indian summer monsoon. These patches of warm water in the SEAS are often referred to as the Arabian Sea Mini Warm Pool (MWP) (Joseph, 1990; Rao and Sivakumar, 1999; Seetaramayya and Master, 1984; Shenoj et al., 1999). The MWP SST remains 0.5 to 1 °C higher than the surroundings during this time. Because the MWP SST stays at more than 30 °C, well above the minimal criteria for deep convection, it is thought to play a significant role in the Indian summer monsoon characteristics over Kerala (Deepa et

al., 2007; Masson et al., 2005; Neema et al., 2012; Rao and Sivakumar, 1999).

Extensive studies have been conducted on the seasonal and interannual evolution of the MWP due to its noteworthy impact on regional climate dynamics (Akhil et al., 2023; Durand et al., 2004, 2007; Kurian and Vinayachandran, 2007; Mathew et al., 2018; Nyadjro et al., 2012; Rao and Sivakumar, 1999; Shenoi et al., 1999). According to Rao and Sivakumar (1999), the East India Coastal Current brings low-salinity water to the SEAS in winter, which causes strong stratification and leads to the formation of the MWP the following May. Shankar and Shetye (1997) explained the formation of the MWP in terms of the wave propagation phenomenon. The downwelling coastal Kelvin wave travels along India's east coast after the summer monsoon has passed, eventually reaching the SEAS in November–December. Later, it is deflected westward by the Rossby Wave, forming the “Laccadive High” (Bruce et al., 1994, 1998; Shankar and Shetye, 1997). The East India Coastal Current, triggered by the coastal Kelvin wave on India's east coast, brings low-salinity water to the SEAS and recirculates along the downwelling Laccadive High eddy in November and December. This low-salinity water leads to the formation of a barrier layer in the SEAS (Gopalakrishna et al., 2005; Hareesh Kumar et al., 2009; Masson et al., 2005; Murty et al., 2006; Shenoi et al., 1999). The barrier layer prevents the mixing of water above and below the thermocline (Lukas and Lindstrom, 1991) and traps the incoming shortwave radiation during the pre-monsoon season within the top few meters and thus increases the SST and leads to the MWP formation in next May (Hastenrath and Greischar, 1989). Masson et al. (2005) reported that the wintertime barrier layer intensifies the SST of the MWP by approximately 0.5 °C.

Hareesh Kumar et al. (2009) investigated the development of the MWP using the Princeton Ocean Model. They stated that salinity has a significant impact on the formation of the MWP. Using an ocean general circulation numerical model, Kurian and Vinayachandran (2007) discovered that the orographic influence of the Western Ghats acts as a wind barrier, increasing net surface heat flux and, hence, MWP intensity. According to Mathew et al. (2018), latent heat flux and incoming shortwave radiation, rather than wintertime freshening, influence the formation of the MWP. Recently, Akhil et al. (2023) found that subsurface dynamics during the preceding winter have very little influence on the development of the MWP.

Warm water can negatively affect the ocean ecosystem, particularly coral reefs (Abram et al., 2003; Doval and Hansell, 2000; Sarma, 2006). Given its proximity, any sudden increase in the intensity of the MWP could impact biological activity in the Laccadive High region. The MWP's impact also affects sound propagation dynamics (Hareesh Kumar et al., 2007). Despite the evident importance, the formation mechanism of the MWP remains a topic of ongoing scientific debate. The complex interplay of fac-

tors contributing to the genesis of the MWP, including winter salinity stratification and the presence of the Western Ghats, has been investigated in previous studies (Durand et al., 2004; Gopalakrishna et al., 2005; Hareesh Kumar et al., 2009; Kurian and Vinayachandran, 2007; Masson et al., 2005; Nyadjro et al., 2012). However, recent findings by Akhil et al. (2023) suggested that the influence of winter salinity stratification on the MWP genesis might be less significant than previously thought. Moreover, a limited number of studies have focused on the air–sea interaction during the mature phase of the MWP, highlighting the need for further research in this area. Hareesh Kumar et al. (2009) and Mathew et al. (2018) have explored these interactions, but comprehensive analyses remain sparse. Li et al. (2023) recently examined the Arabian Sea warm pool during its mature phase, emphasizing its seasonal and interannual variability using reanalysis datasets. While these studies contribute valuable insights, they primarily address variability over time rather than the specific processes driving the MWP's development and dissipation.

In this study, we examine the impact of the air–sea interaction on the progression of the Arabian Sea Mini Warm Pool using a coupled atmosphere–ocean numerical model. The coupled model employed in this study is calibrated for precise application on a seasonal timescale, which imposes limitations on the duration of simulations. Therefore, long-term simulations in each year are not feasible. Consequently, the present study focuses on configuring a regional coupled atmosphere–ocean numerical model to study the region-specific expansion and dissipation of the MWP. We also aim to elucidate the contribution of oceanic and atmospheric conditions to its growth over the years with distinct MWP intensity. The primary framework of the study is as follows: Sect. 2 provides an in-depth discussion of the data and methodology, including a detailed explanation of the coupled numerical model. Section 3 demonstrates the results along with the coupled model's ability to simulate temperature, salinity, and currents. Further, a few model sensitivity experiments have been incorporated to explore MWP characteristics and the influence of atmospheric and oceanic conditions across three different MWP events. Section 4 discusses the results and concludes the study with key findings.

2 Data and methodology

2.1 Data

We utilized the Advanced Very High Resolution Radiometer (AVHRR) SST dataset, which is a part of the NOAA Climate Data Record program product suite. This dataset combines in situ and satellite data from 1981 to the present using the optimal interpolation approach and is available at a daily timescale with a spatial resolution of 0.25° (Banzon et al., 2016). In this study, the coupled model's simulated

SST is compared with the daily AVHRR SST data for the years 2013, 2016, and 2018. We used weekly sea surface salinity (SSS) data from the European Space Agency's Sea Surface Salinity Climate Change Initiative (CCI) to validate the model's simulated sea surface salinity (SSS). This global Level 4 dataset is derived from a multi-sensor combination (SMOS, Aquarius, and SMAP). It spans from 2010 to 2020, offering a horizontal resolution of 50 km and a weekly temporal frequency (Boutin et al., 2021). The model's ability to reproduce ocean surface currents is confirmed using OSCAR surface current data with a horizontal resolution of 0.33° and a temporal resolution of 5 d (Bonjean and Lagerloef, 2002). The numerical model-simulated vertical temperature and salinity are compared against AD10 buoy measurement data. AD10 is a moored buoy, and the National Institute of Ocean Technology (NIOT) is entrusted to deploy and collect the moored buoy data, later made available via the Indian National Centre for Ocean Information Services (INCOIS) data portal (<https://incois.gov.in/portal/datainfo/mb.jsp>, last access: 6 June 2024). The vertical resolution of the buoy data varies with depth.

2.2 Model details

The coupled atmosphere–ocean numerical model consists of the atmospheric model Advanced Research Weather Research and Forecasting (WRF–ARW) and the ocean model Regional Ocean Modeling System (ROMS). Both models are part of the Coupled Ocean–Atmosphere–Wave–Sediment Transport Modeling System (COAWST) (Warner et al., 2010). The model coupling toolkit (MCT) is used to couple the atmospheric model WRF–ARW and ocean model ROMS (Jacob et al., 2005). Previously, this coupled numerical model was used to study the air–sea interaction during tropical cyclones (Chakraborty et al., 2022; Prakash et al., 2018; Prakash and Pant, 2017, 2020; Zambon et al., 2014), coastal processes (Carniel et al., 2016; Olabarrieta et al., 2011, 2012; Ricchi et al., 2016), and monsoon deep depressions over the Bay of Bengal (Chakraborty et al., 2023).

The ROMS model is a free-surface, hydrostatic, three-dimensional primitive equation (i.e. Reynolds-averaged Navier–Stokes equation) ocean model widely used in estuarine, coastal, and basin-scale research. The primitive equations in the ROMS model are solved using boundary-fit orthogonal curvilinear coordinates on a staggered Arakawa C grid (Arakawa and Lamb, 1977). This model employs a terrain-following vertical sigma coordinate system (Haidvogel et al., 2000; Phillips, 1957; Song and Haidvogel, 1994) and incorporates a variety of advection techniques, such as second- and fourth-order center differences and third-order upstream biased method. Vertical mixing in ROMS is handled using either the local generic length scale closure technique (Umlauf and Burchard, 2003) or the nonlocal k -profile boundary layer formulation (Large et al., 1994). Horizontal mixing of momentum and tracers can occur at vertical levels

or geopotential or isopycnal surfaces. Due to its very accurate and efficient physical and numerical algorithms, the ROMS model has been widely used to investigate the coastal, open-ocean, and biogeochemical processes (Nigam et al., 2018; Paul et al., 2023; Sandeep et al., 2018; Seelanki et al., 2021).

The WRF–ARW atmospheric model is a non-hydrostatic fully compressible model that predicts mesoscale processes using boundary layer physics schemes and various physical parameterizations (Skamarock and Klemp, 2008; Skamarock et al., 2008). On a horizontal Arakawa C grid and a vertical sigma-pressure coordinate, WRF–ARW estimates the wind momentum components, surface pressure, longwave and shortwave radiative fluxes, dew point, precipitation, surface sensible and latent heat fluxes, relative humidity, and air temperature. WRF is intended to serve and support atmospheric research and operational forecasting needs (Dai et al., 2013). Parameterization schemes are available in microphysics, cumulus parameterization, planetary boundary layer, surface layer, land surface, and longwave and shortwave radiations, with multiple options for each process. In the COAWST modeling system, the WRF code was modified to provide improved bottom roughness when computing bottom stress over the ocean (Warner et al., 2010). In addition to WRF and ROMS, the COAWST modeling framework also consists of wave and sediment transport models; however, these components are not used in this study.

2.3 Model configuration and experiment design

The atmospheric component of the coupled numerical model (i.e. WRF model) supports a variety of parameterization schemes. In our WRF configuration, we have incorporated the WRF Single-Moment 6-Class Scheme (Lim and Hong, 2010) as microphysics parameterization to represent grid-scale precipitation processes, the New Tiedtke scheme for cumulus parameterization that illustrates sub-grid-scale convection and cloud detrainment (Zhang and Wang, 2017), the Yonsei University Scheme (Hong et al., 2006) for planetary boundary layer physics, and the MM5 Similarity Scheme (Paulson, 1970). We have used the Unified Noah Land Surface Model (Tewari et al., 2004). At each time step, the atmospheric and land surface models calculate exchange coefficients and surface fluxes of the land or ocean layer and send them to the Yonsei University planetary boundary layer (Hong et al., 2006). The Dudhia shortwave scheme (Dudhia, 1989) is used for shortwave radiation parameterization, and the RRTM scheme (Mlawer et al., 1997) is used for longwave radiation parameterization. The WRF domain has an outer domain resolution of 60 km (18° S to 38° N and 25 to 95° E) and a nested domain with a 1 : 3 ratio (Fig. 1). It consists of 40 levels in the vertical direction. WRF is initialized with ERA5 data (Hersbach et al., 2020). The outer domain's lateral boundary condition is taken from ERA5 at 3 h intervals.

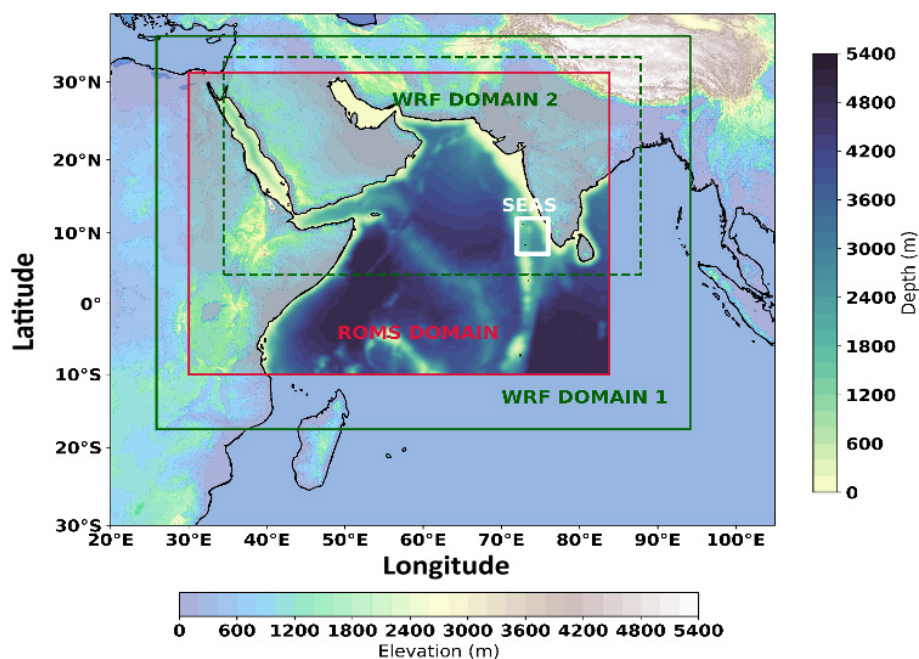


Figure 1. WRF and ROMS model domains. The WRF domain is the green box, while the red box shows the ROMS model domain. Two domains of WRF are shown in solid and dashed green lines. The white box is the southeastern Arabian Sea (core area of the MWP). Land elevation and ocean depth are shown in two different contours.

The ocean model ROMS employed in this study covers the Arabian Sea spanning 10°S – 30°N and 30° – 85°E with a horizontal resolution of $\frac{1}{6}$. A terrain-following sigma coordinate system with 40 vertical levels was used, 20 of which are concentrated in the upper 200 m. The ETOPO2 with 2 arc min resolution data has been used to create the bathymetry data over the ROMS grid. The surface and bottom stretching parameters for sigma coordinates were set to $\theta_s = 7$ and $\theta_b = 1.5$, with a critical depth of 10 m. The initial conditions and lateral boundary forcings for ROMS were derived from SODAv3.4.2 (Carton et al., 2018) data, with a horizontal resolution of $0.5^{\circ} \times 0.5^{\circ}$ and a temporal availability of 5 d interval. Momentum and tracer particles were mixed horizontally along the geopotential surface. The nonlocal K -profile parameterization scheme (Large et al., 1994), which integrates the different unresolved processes associated with vertical mixing, was used to deal with vertical mixing. Horizontal and vertical advection of momentum were treated using third-order upstream and fourth-order centered advection schemes, respectively. The ROMS model employed 60 s baroclinic and 30 s barotropic time steps. Open boundary conditions for momentum and tracers on the southern and eastern boundaries used radiation schemes, allowing remote forcings from the Bay of Bengal and the southern Indian Ocean to influence the domain. Northern and western boundaries were closed in the ROMS model. Both models were initialized from April and simulated until June. A 1-month spin-up period was sufficient to establish the mixed-layer dynamics (the MWP extends till the mixed-layer depth; see Fig. S10).

From the previous studies and our own experience (based on our several background experiments), we have observed that the coupled atmosphere–ocean numerical model (part of the COAWST model) would be more accurate if the simulation was up to the seasonal scale. Therefore, to assess the MWP using this coupled model, we ran the model for about 80 d for three independent years (2013, 2016, and 2018) which had distinct MWP characteristics (based on the inter-annual variation of the MWP area; see Fig. S1 in the Supplement). At every 15 min, the WRF and ROMS models interchange variables. While SST is the sole variable that is transferred from ROMS to WRF, other parameters, including 2 m air temperature, mean sea level pressure, 10 m u and v wind velocity, longwave and shortwave radiation, rainfall, and relative humidity, are exchanged between WRF and ROMS (readers are referred to Warner et al., 2010, for more details regarding the coupled model). Each run is initialized separately on 1 April and run to 20 June each year, and the output is saved at a daily frequency. The first month of each simulation was used for spin-up and is not included in the analysis (except for the mixed-layer heat budget analysis; Fig. 11). We named this set of runs the control experiment (CNTRL), where we used the SODA and ERA5 data for actual oceanic and atmospheric conditions. Later, to investigate the factors contributing to the evolution of the MWP, we designed and performed four idealized numerical experiments using the coupled atmosphere–ocean model with a one-way coupling mode. We modified the oceanic and atmospheric conditions in these experiments as detailed in Table 1. In 2018, the

Table 1. List of model sensitivity experiments.

Experiment name	Ocean model initial and boundary forcing year	Atmospheric forcing year
Control	2018	2018
S _{ocean2013}	2013	2018
S _{atmos2013}	2018	2013
S _{ocean2016}	2016	2018
S _{atmos2016}	2018	2016

MWP area was closer to climatology (Fig. S1). Hence, this year is used as the base year, and in all four sensitivity experiments, the forcings of the two other years are fed into the 2018 control run.

2.4 Mixed-layer heat budget

The mixed-layer heat budget provides a detailed analysis of factors that can contribute to the change in the mixed-layer temperature and is calculated using the formula outlined in Akhil et al. (2023), Foltz and McPhaden (2009), Girishkumar et al. (2017), Nyadjro et al. (2012), Prakash and Pant (2017), Stevenson and Niiler (1983), and Vialard et al. (2008), and it is given as follows:

$$\frac{\partial T}{\partial t} = \frac{Q_{net}}{\rho C_p h} - \left(u \frac{\partial T}{\partial x} + v \frac{\partial T}{\partial y} \right) + H \left[W_{-h} + \frac{\partial h}{\partial t} \right] \left[\frac{T_h - T}{h} \right] + \text{residuals.} \tag{1}$$

Different terms in the above equation’s right-hand side (RHS) contribute to temperature tendency differently; the first term on the RHS is the contribution from net surface heat flux, the second is from horizontal advection, and the third is from vertical process and entrainment. *T* is the average temperature of the mixed layer, *t* is the time (in days), and *h* is the mixed-layer depth (MLD). Meridional and zonal velocities at MLD are given by *u* and *v*. *Q_{net}* is the net surface heat flux. Here, we have not considered the penetrative shortwave radiation below the MLD. *H* is the Heaviside step function and is expressed as *H* = 0 if $[W_{-h} + \frac{\partial h}{\partial t}] < 0$ or *H* = 1 if $[W_{-h} + \frac{\partial h}{\partial t}] > 1$. *W_{-h}* is the vertical velocity. *T_h* is the temperature just below (5 m) the depth of the MLD. The residual term represents contributions from other processes, such as diffusion. The units of all the terms here are in °C d⁻¹. In this study, the depth at which the subsurface temperature decreases by 1 °C as compared to the surface is used as the isothermal-layer depth (ILD) (Kara et al., 2000; Shee et al., 2019; Sprintall and Tomczak, 1992). The MLD is calculated following Shee

et al. (2019) as follows:

$$\sigma_{t(z=h)} = \sigma_{t(z=0)} + \Delta T \frac{d\sigma_t}{dT},$$

where Δ*T* is the 1 °C temperature criteria for ILD and $\frac{d\sigma_t}{dT}$ is the coefficient of thermal expansion.

2.5 The production of turbulent kinetic energy (*P_{TKE}*)

The production of turbulent kinetic energy (*P_{TKE}*) is used to understand the convective mixing caused by the relative contributions of wind stress (wind-forced momentum flux), freshwater flux (*E* – *P*) (haline buoyancy flux), and net surface heat flux (thermal buoyancy flux) (Shankar et al., 2016). *P_{TKE}* is calculated using the expression given in Han et al. (2001) and Rao et al. (2002) and expressed as follows:

$$P_{TKE} = \rho u_*^3 + \left[-\frac{\alpha 0.5 g k MLD Q_{net}}{C_p} + 0.5 \rho g k MLD \beta (E - P) S_0 \right],$$

where $u_* = \sqrt{\frac{\tau}{\rho}}$ is the frictional velocity, τ is the wind stress, ρ is the density of the seawater (1026 kg m⁻³), *k* = 0.42 is the von Kármán constant, and *g* is the acceleration due to gravity. *E* is the evaporation rate, and *P* is the precipitation. *S₀* is the salinity of the ML. *Q_{net}* is the net surface heat flux. The thermal expansion coefficient (α) and haline contraction coefficient (β) are taken to be $\alpha = -0.00025 \text{ K}^{-1}$ and $\beta = 0.00785 \text{ psu}^{-1}$, respectively, following studies by Shankar et al. (2016) and He et al. (2020). *C_p* (= 4187 J kg⁻¹) is the ocean’s specific heat capacity. The first term on the right-hand side of the above equation represents *P_{TKE}* due to wind stirring. The first term in the bracket is the *P_{TKE}* due to thermal buoyancy representing the effect of net surface heat flux, and the second term is *P_{TKE}* due to the haline buoyancy, which indicates the impact of freshwater change. The wind-stirring term, by definition, cannot be negative. A positive thermal buoyancy flux implies that heat is lost from the ocean, which causes MLD to deepen. On the other hand, the positive haline buoyancy flux causes more evaporation, which leads to an increase in MLD due to increased salinity (He et al., 2020; Shankar et al., 2016; Shee et al., 2019).

3 Results

3.1 Model validation

Figures 2–4 compare the coupled model’s simulated SST, SSS, and current to observation data in 2018, 2013, and 2016. The mean results and bias are then shown for each of the three years from 1 May to 20 June. The simulated SST effectively captured the cold SST along the Somali coast across all the examined years, firmly aligning with AVHRR SST data (Fig. 2). The SST bias remained within 1.5–2 °C in all

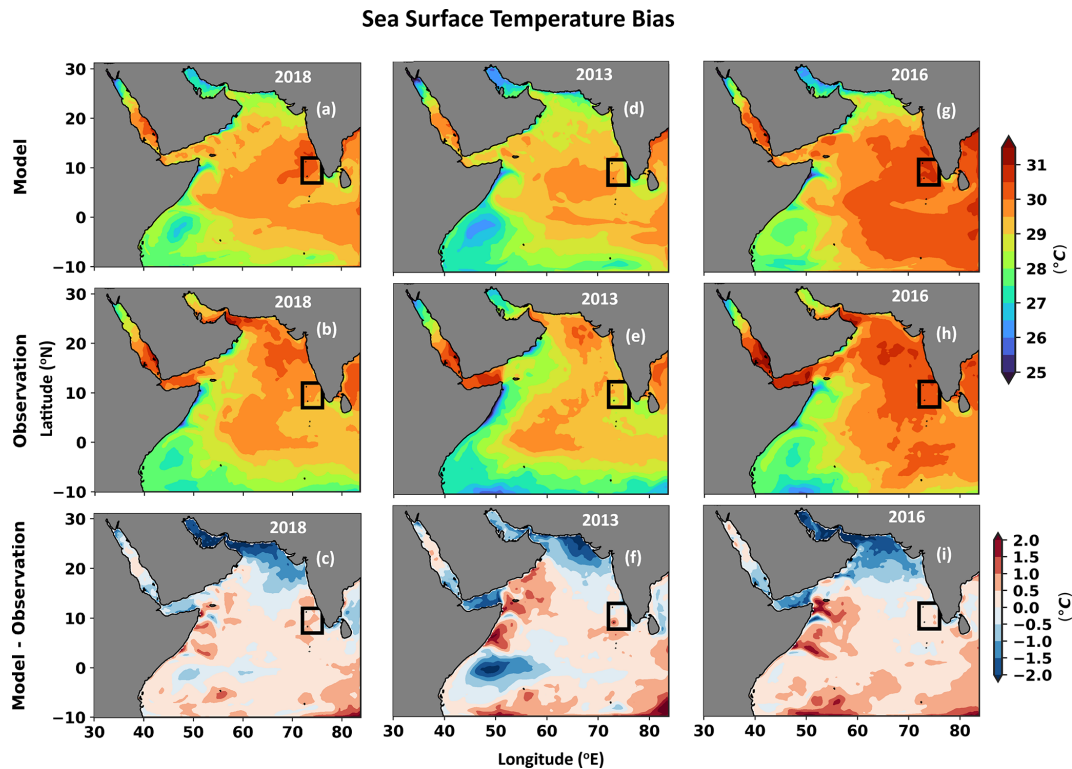


Figure 2. Comparison of model-simulated sea surface temperature (SST) and NOAA-AVHRR surface temperature. Panels (a), (d), and (g) depict model-simulated SST for the years 2018, 2013, and 2016, respectively. Panels (b), (e), and (h) display NOAA-AVHRR SST for the corresponding years. Panels (c), (f), and (i) illustrate the SST difference between model output and observation. The black box delineates the domain of interest, i.e. the MWP core region. The mean results and bias are shown for each of the three years, averaged from 1 May to 20 June.

three experiments except in the northern Arabian Sea and along the Somali coast. In the north Arabian Sea, a cold SST bias and a warm SST bias near the Somali coast of more than $1\text{ }^{\circ}\text{C}$ are observed. In the tropical western Indian Ocean, a cold SST bias was also witnessed in 2013. Despite this, the SST bias remained consistent across the study period, with a minimal bias in the SEAS region (black box in Fig. 2). The model-simulated surface salinity revealed a pronounced high-salinity tongue in the northern Arabian Sea, a feature similarly observed in the ESA salinity data (Fig. 3). The coupled model effectively reproduced the low-salinity water in the SEAS, with the salinity bias being primarily within 0.5 psu across the entire domain, except for a few isolated areas reaching 1 psu . The Indian Ocean is well known for its seasonally reversing monsoon current. The West India Coastal Current (WICC) transports high-salinity water from the northern to the southern Arabian Sea in May and June and is the primary driver of inter-basin mass transport (Schott et al., 2009; Schott and McCreary, 2001; Shankar et al., 2002). The model-simulated surface currents accurately captured the WICC between May and June for all three years (Fig. 4). Furthermore, the representation of the summer mon-

soon current in the simulation was commendable (not shown here).

The coupled model's temperature and salinity profiles were confirmed against buoy measurements at the AD10 location (10.25° N , 72.25° E) (Fig. S2). We utilized the model's nearest point to the AD10 location to serve this purpose. Before validation, the model-simulated data are interpolated to the vertical resolution of the AD10 buoy data. The AD10 buoy data were available at an hourly timescale from 2012 to 2020 and at a 3 h frequency in 2021. Except for 2016, the AD10 temperature contains data gaps (Figs. S3–S5). In 2018, the model temperature had a cold bias below 50 m depth at the buoy location. In 2013 and 2016, the model's simulated temperature had a positive bias of less than $1\text{ }^{\circ}\text{C}$ within the top 50 m. Although the vertical temperature is consistent with the AD10 buoy data, the model-simulated salinity data indicated more discrepancies in 2018. Aside from that, the model's represented salinity stayed within 1 psu bias in 2013 and 2016, with only a few areas exceeding this limit in 2013. The MWP does not extend beyond the mixed-layer depth (Akhil et al., 2023, and Fig. S10), and our model-estimated temperature and salinity remain in excellent accord within this depth. To further examine the vertical temperature per-

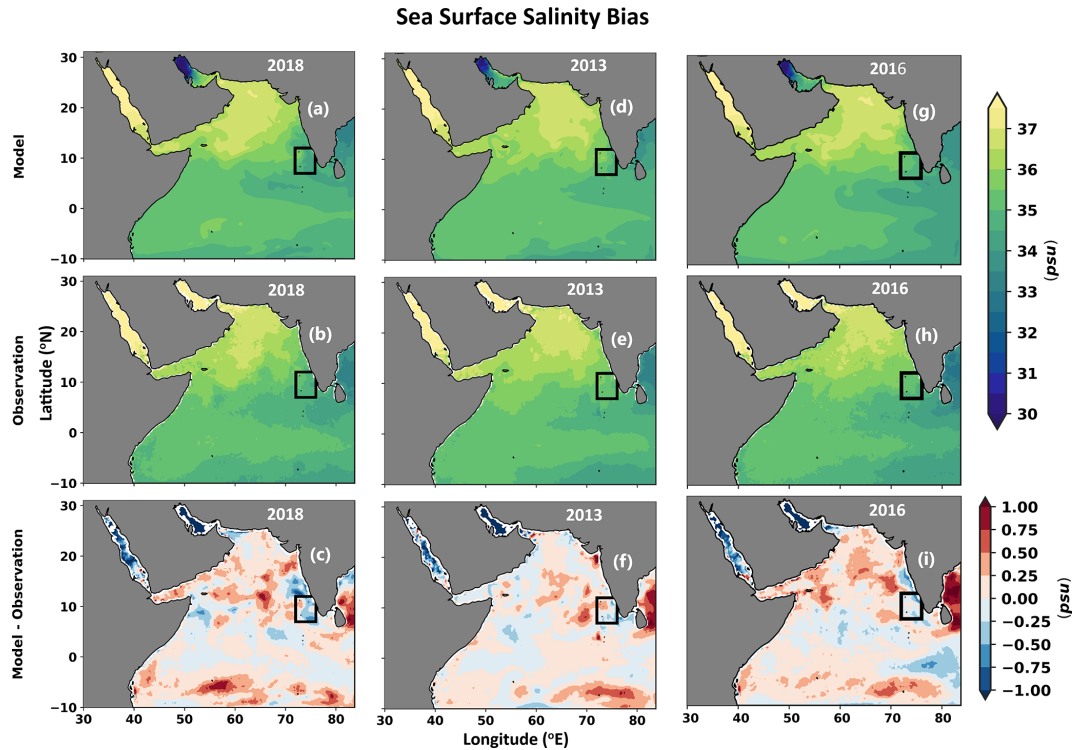


Figure 3. Comparison of model-simulated sea surface salinity (SSS) and ESA-observed SSS. Panels (a), (d) and (g) depict model-simulated SSS for the years 2018, 2013, and 2016, respectively. Panels (b), (e), and (h) display observed SSS for the corresponding years. Panels (c), (f), and (i) illustrate the SSS difference between the model output and observation. The black box delineates the domain of interest, i.e. the MWP core region. The mean results and bias are shown for each of the three years, averaged from 1 May to 20 June.

formance of the model, we conducted a detailed temporal correlation analysis of the simulated temperatures for three distinct control experiments corresponding to the years 2018, 2013, and 2016. This analysis is performed against observational data obtained from the AD10 buoy location, with calculations made at various depths, specifically at 1, 5, 10, 15, 20, 30, 50, and 100 m. The results of this statistical assessment are graphically represented in a Taylor diagram (Fig. 5). The points at 50 m depth are out of the range of axes for 2013. Across all three control experiments, the standard deviation of the simulated temperature values generally ranged between 0.3 and 1.5, with a few exceptions at certain depths. Additionally, the correlation coefficient between the model simulations and the buoy observations varied from 0.5 to 0.98, indicating a moderate to strong agreement depending on the depth considered.

3.2 Ocean surface characteristics during various phases of the Arabian Sea Mini Warm Pool

Figure 6 shows the model-simulated SST, wind stress, and salinity during the mature and dissipation days of the MWP. The mature day of the MWP is characterized by the day when SST within the MWP core (shown by the white box in Fig. 1) reaches its highest magnitude in May (Table 2). The

dissipation day is determined when the MWP SST equates that of the surrounding water following its mature phase. In addition, the days from the mature to the dissipation day are termed the dissipation phase. Previous studies (Li et al., 2023; Rao and Sivakumar, 1999; etc.) have used 30 °C to identify the MWP. A consistent bias of 0.5 °C is noticed in SEAS; hence, our study used a threshold of 30.5 °C to detect the MWP. In 2018, the SST within the MWP core reached above 31 °C on 20 May, after which it gradually decreased (Fig. 6a–c). During the mature day in 2018, wind stress over the SEAS was low compared to its surroundings, but wind speed increased considerably afterward. Subsequently, the MWP SST matched the temperature of the surrounding sea by 8 June. Despite the absence of the MWP in 2013, the same MWP mature and dissipation day as in 2018 was used for demonstrative purposes (as shown in Fig. 6d–f). In 2016, the MWP matured on 4 May with a larger spatial area than the previous two years (Fig. 6g–i). During the mature day, the wind stress was minimal in the southern Arabian Sea (Fig. 6g). Once the wind stress escalated, the MWP entirely dissipated by 6 June 2016 (Fig. 6h and i).

Salinity in the vicinity of the MWP was lower during its mature day (< 34 psu except in 2013) but increased during its dissipation day (> 35.2 psu) (Fig. 7a–i). In the MWP core region, salinity was notably lower in 2018 compared to the

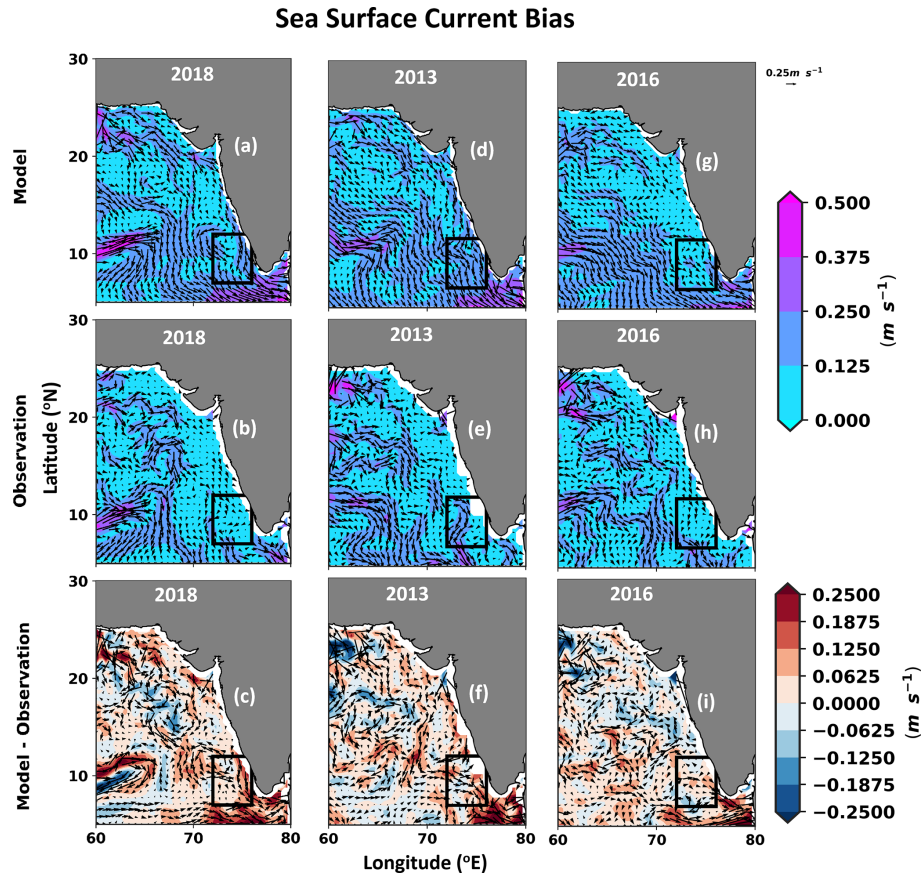


Figure 4. Comparisons of model simulated currents against OSCAR surface current. The first column from the left (a–c) is for 2018, the second is for 2013 (d–f), and the last is for 2016 (g–i). As the MWP forms near the western coast of India, the current patterns are shown in the adjacent region and not the whole model domain. Panels (c), (f), and (i) illustrate the difference between the resultant current and the direction between model output and observation. The black box delineates the domain of interest, i.e. the MWP core region. The mean results and bias are shown for each of the three years, averaged from 1 May to 20 June.

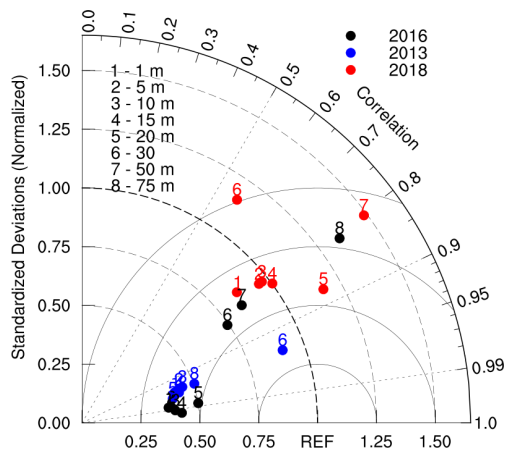


Figure 5. Taylor diagram showing the temporal correlation and standard deviations of the model-simulated temperature profile from the three years of model experiments with respect to measurements at the buoy AD10.

Table 2. Details of mature and dissipation days in each year with the threshold used to identify the MWP.

Year	Mature day	Dissipation day	Threshold
2018	20 May	8 June	30.5 °C
2013	20 May	8 June	30.5 °C
2016	4 May	6 June	30.5 °C

other two years (Fig. 7a). In 2016, while the MWP was in its mature stage, low-salinity water (less than 34 psu) was detected south of SEAS, slightly outside the core MWP area (Fig. 7g). The salinity was higher in the SEAS during the mature day in 2013 as compared to 2016 and 2018.

On the mature day of the MWP, there was a positive net surface heat flux across the Arabian Sea except for its southern flank (Fig. 8a, d, and g). However, as wind stress intensified during the dissipation phase, the net surface heat flux in the Arabian Sea transitioned to negative values in all the

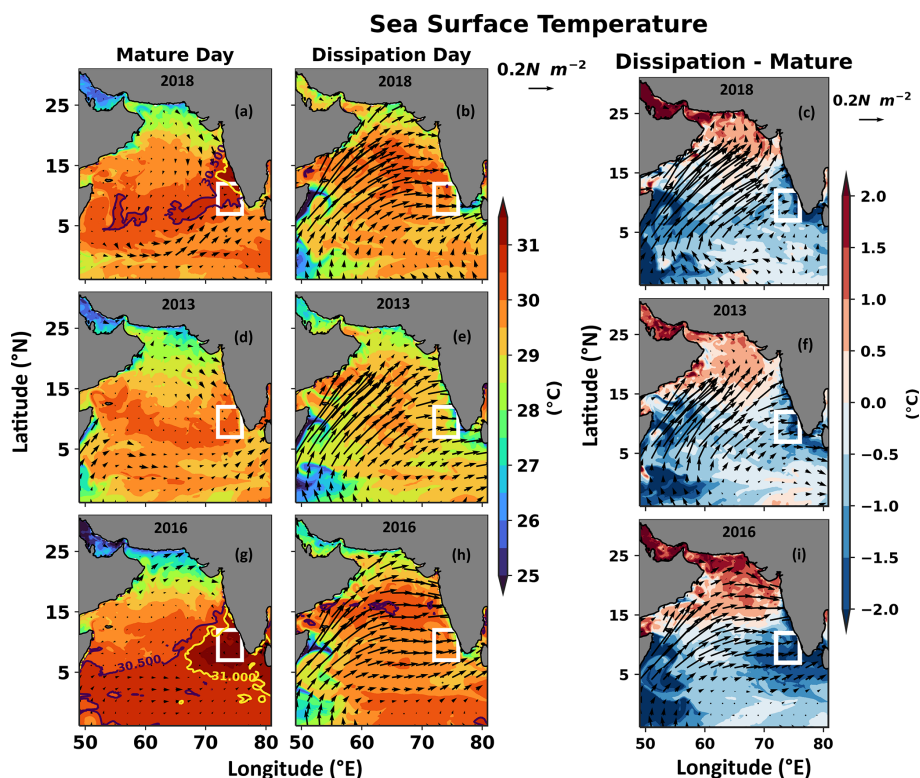


Figure 6. Comparison of SST overlaid by wind stress on mature and dissipation days (see Table 2 for details) in 2018 (a–c) (MWP strength close to climatology), 2013 (d–f) (MWP was absent), and 2016 (g–i) (MWP was intense). (c), (f), and (i) show the distinction between dissipation and mature days. The MWP's mature days are 20 May 2018, 20 May 2013, and 4 May 2016. The MWP's dissipation days are 8 June 2018, 8 June 2013, and 6 June 2016. The black and yellow contours represent 30.5 and 31 °C, respectively. The white box is the core MWP region.

years (Fig. 8c, f, and i). Subsequently, four elements of the net surface heat flux are examined to understand its impact on the regional growth of the MWP in SEAS (Figs. S6–S9). The shortwave radiation flux was positive and contributed majorly to the net surface heat flux. Because of the clear sky, the shortwave radiation was higher in April–May (Li et al., 2023). However, once the southwesterly wind strengthened, the subsequent cloudiness blocked the incoming shortwave radiation flux. Consequently, the shortwave radiation flux in the SEAS reduced on dissipation day (Fig. S6c, f, and i). The exchange of energy between the atmosphere and ocean is facilitated by turbulent processes, such as sensible and latent heat flux (Large and Pond, 1981). As the wind speed increased, the loss of the latent heat flux increased from the mature to the dissipation day in all the years (Fig. S8c, f, and i).

3.3 Causative factors

3.3.1 The role of the atmosphere and ocean in the formation of the MWP

This section examines the relative contributions of the ocean and atmosphere to the development of the MWP through

four sensitivity experiments (see Table 1 for details). In the $S_{\text{ocean2013}}$ and $S_{\text{ocean2016}}$ experiments, the ocean initial and boundary conditions from 2013 and 2016 replace those in the 2018 control experiment, respectively. The MWP remains very strong (weak) in the $S_{\text{ocean2016}}$ ($S_{\text{ocean2013}}$) experiment and reaches its maximum extent on 20 May (Fig. 9a and b are compared with Fig. 9c). An intense MWP was developed in the 2016 control experiment, and a similar MWP is also seen in $S_{\text{ocean2016}}$. The initial mean pre-April ocean temperature in SEAS (initial condition temperature is averaged within the white box in Figs. 9 and 10 and to the MLD) was 0.35 °C higher in 2016 (0.15 °C lower in 2013) compared to 2018. Following the initial conditions, the MWP core temperature within the MLD was 0.6 °C higher in $S_{\text{ocean2016}}$ (0.3 °C lower in $S_{\text{ocean2013}}$) compared to the 2018 control simulation during the mature day (Fig. S10d and e are compared with Fig. S10a). These results indicate that the pre-April ocean conditions strongly influence the intensity of the MWP.

Later, in the $S_{\text{atmos2013}}$ experiment, the 2013 atmospheric conditions were replaced with the 2018 control experiment's atmospheric conditions. The MWP is absent in the 2013 control and $S_{\text{atmos2013}}$ experiments (Figs. 10a and 6d). Similarly, the 2016 atmospheric conditions replace those used in the

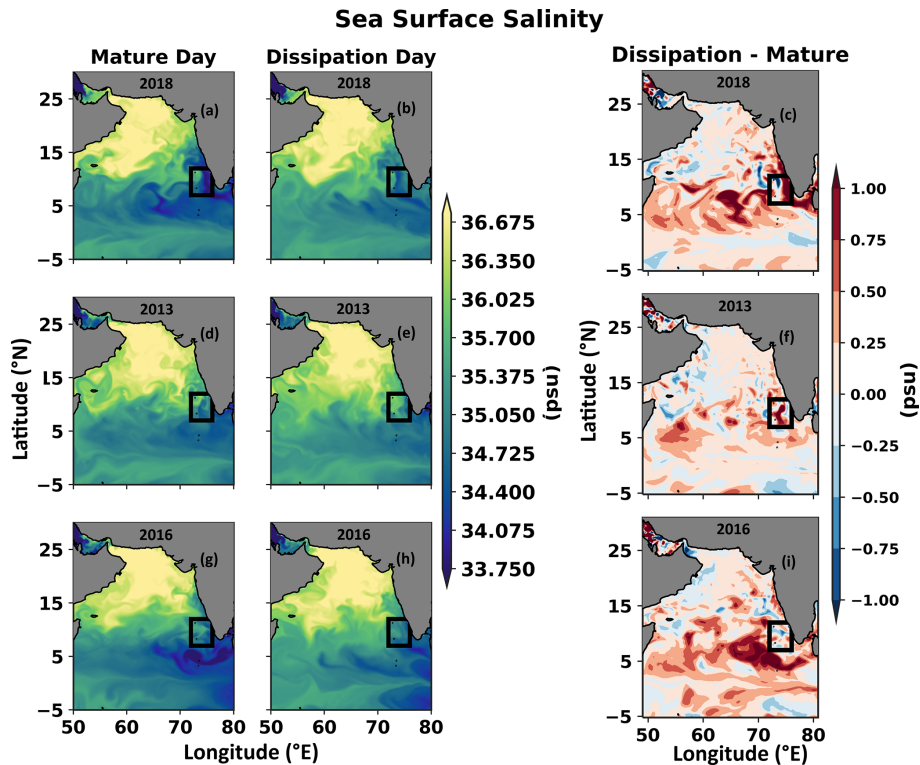


Figure 7. Comparison of sea surface salinity on mature and dissipation days (see Table 2 for details) in 2018 (a–c) (MWP strength close to climatology), 2013 (d–f) (MWP was absent), and 2016 (g–i) (MWP was intense). (c), (f), and (i) show the distinction between dissipation and mature day. The MWP's mature days are 20 May 2018, 20 May 2013, and 4 May 2016. The MWP's dissipation days are 8 June 2018, 8 June 2013, and 6 June 2016. The black box is the core MWP region.

2018 control experiment, which is termed the $S_{\text{atmos}2016}$ experiment. A strong MWP was observed in the $S_{\text{atmos}2016}$ experiment (Fig. 10b), albeit with a lower intensity than in the 2016 control (Fig. 6g) and $S_{\text{ocean}2016}$ (Fig. 9b) experiment, indicating that pre-April ocean conditions were responsible for the formation of an intense MWP in the 2016 control experiment. In the $S_{\text{atmos}2016}$ and 2016 control experiments, the MWP matured on 4 May. Similarly, the $S_{\text{ocean}2016}$ and 2018 control experiments have analogous atmospheric conditions, and the MWP matures on 20 May (Fig. 9b and c). These findings suggest that the atmospheric variables determine the spatial variability in the MWP as well as the day of maturation.

The mixed-layer heat budget in the core region of the MWP (72–76°E and 7–13°N) is analyzed to allow for a better understanding of the factors contributing to its expansion and dissipation. The atmospheric conditions remain unchanged in the $S_{\text{ocean}2013}$, $S_{\text{ocean}2016}$, and 2018 control experiments. A dip in the net surface heat flux from 0.1 to -0.07 °C d⁻¹ is noticed on 8 May in these three experiments. Later, this net surface heat flux supplied to the mixed-layer temperature tendency with a maximum of 0.1 °C d⁻¹ from 15 to 18 May (Fig. 11a, d, and e), and the MWP matured on 20 May thereafter. During the dissipation phase of the MWP,

the net surface heat flux had an adverse impact on the temperature tendency in $S_{\text{ocean}2013}$, $S_{\text{ocean}2016}$, and 2018 control experiments. The vertical processes also had a cooling effect on the temperature tendency, which peaked at -0.09 °C d⁻¹ on 26 May in $S_{\text{ocean}2013}$, $S_{\text{ocean}2016}$, and 2018 control experiments. Even if the MWP was not apparent in the 2013 and $S_{\text{atmos}2013}$ experiments (both of these experiments have similar atmospheric conditions), the net surface heat flux caused a gain of 0.05 °C in temperature within the mixed layer on 20 May (Fig. 11b and f). Once the MWP reached its mature day, the vertical processes and the net surface heat flux had a detrimental effect on the temperature tendency in the $S_{\text{atmos}2016}$ and 2016 control experiments (Fig. 11c and g). In all control and sensitivity experiments, the temperature tendency is negatively impacted by the vertical processes during May and June; nevertheless, the net surface heat flux is the primary driver behind the variation of the temperature tendency from the mature to the dissipation day. The horizontal advection had very minimal influence on the temperature tendency. Thus, atmospheric conditions modulate the mature and dissipation of the MWP.

To better assess the atmosphere's and ocean's relative contribution to the MWP intensity across different experiments, we introduced the MWP intensity index. This index is de-

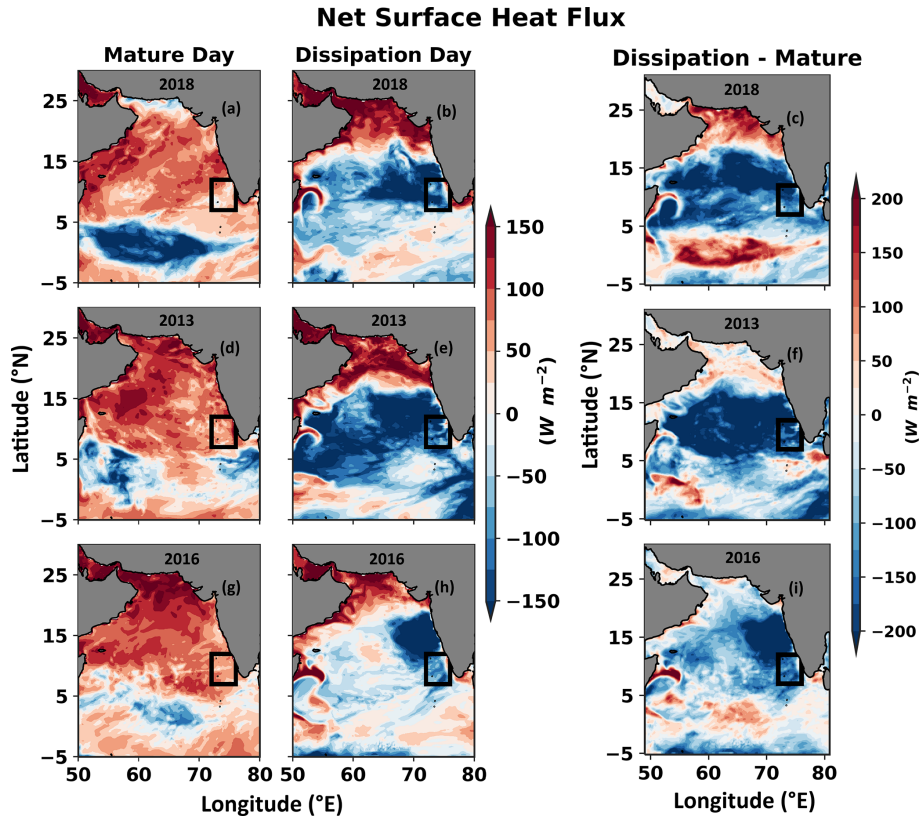


Figure 8. Same as Fig. 7 but for net surface heat flux.

fined as follows:

$$\text{MWP intensity index} = \text{MWP area on mature day} \times \Delta T_{\text{avg}}$$

where ΔT_{avg} represents the average temperature change within the MWP area from its initial condition to the mature day.

In the 2016 control experiment, the MWP intensity index reached its highest value, corresponding to the warmest MWP SST and the most extensive area (Fig. 12). In contrast, the MWP was weak in the 2013 control experiment, and so was the MWP intensity index. In the $S_{\text{ocean2013}}$ experiment, where the ocean's initial and boundary conditions were modified from 2018 to 2013, the MWP intensity index decreased by 8.5 % compared to the 2018 control experiment. However, a substantial reduction of 82 % in the MWP intensity index was found when the atmospheric forcings were altered to 2013 in the $S_{\text{atmos2013}}$ experiment, highlighting the adverse effect of the atmospheric environment on the formation of the MWP.

Conversely, the $S_{\text{ocean2016}}$ experiment, which replaced the 2018 oceanic initial and boundary condition with that of 2016, showed a 136 % rise in the MWP intensity index compared to the 2018 control experiment. However, when the atmospheric condition was adjusted to 2016 in the $S_{\text{atmos2016}}$ experiment, the MWP intensity index decreased

by 41 %, indicating that the ocean precondition was the primary factor in the genesis of the intense MWP in 2016 and that the atmospheric condition later favored its development (Fig. 12).

3.3.2 Impact of ocean surface flux on the formation of the MWP

Once the ocean precondition was met, the atmospheric factors, including net surface heat flux, wind, and freshwater flux, played a leading role in shaping the spatial extent of the MWP. The relative importance of net thermal flux, freshwater flux, and wind on mixing is examined here using production of turbulent kinetic energy (P_{TKE}). Contrary to wind stirring, the P_{TKE} by haline and thermal buoyancy flux was of smaller magnitude in all the experiments, indicating that the wind was the driver for the mixing in SEAS in May (Fig. 13). The atmospheric conditions were similar in the 2018 control, $S_{\text{ocean2013}}$, and $S_{\text{ocean2016}}$ experiments (see Table 1 for experiment details). From 1 to 5 May, the average P_{TKE} caused by wind stirring was more than 8 W m^{-2} ; however, in the SEAS, a small wind shadow zone was formed with a very low P_{TKE} (Fig. 14a). Subsequently, the mixing reduced, and expansion of MWP SST was observed within this wind shadow zone in 2018 control, $S_{\text{ocean2013}}$, and $S_{\text{ocean2016}}$ experiments. A similar but much wider wind

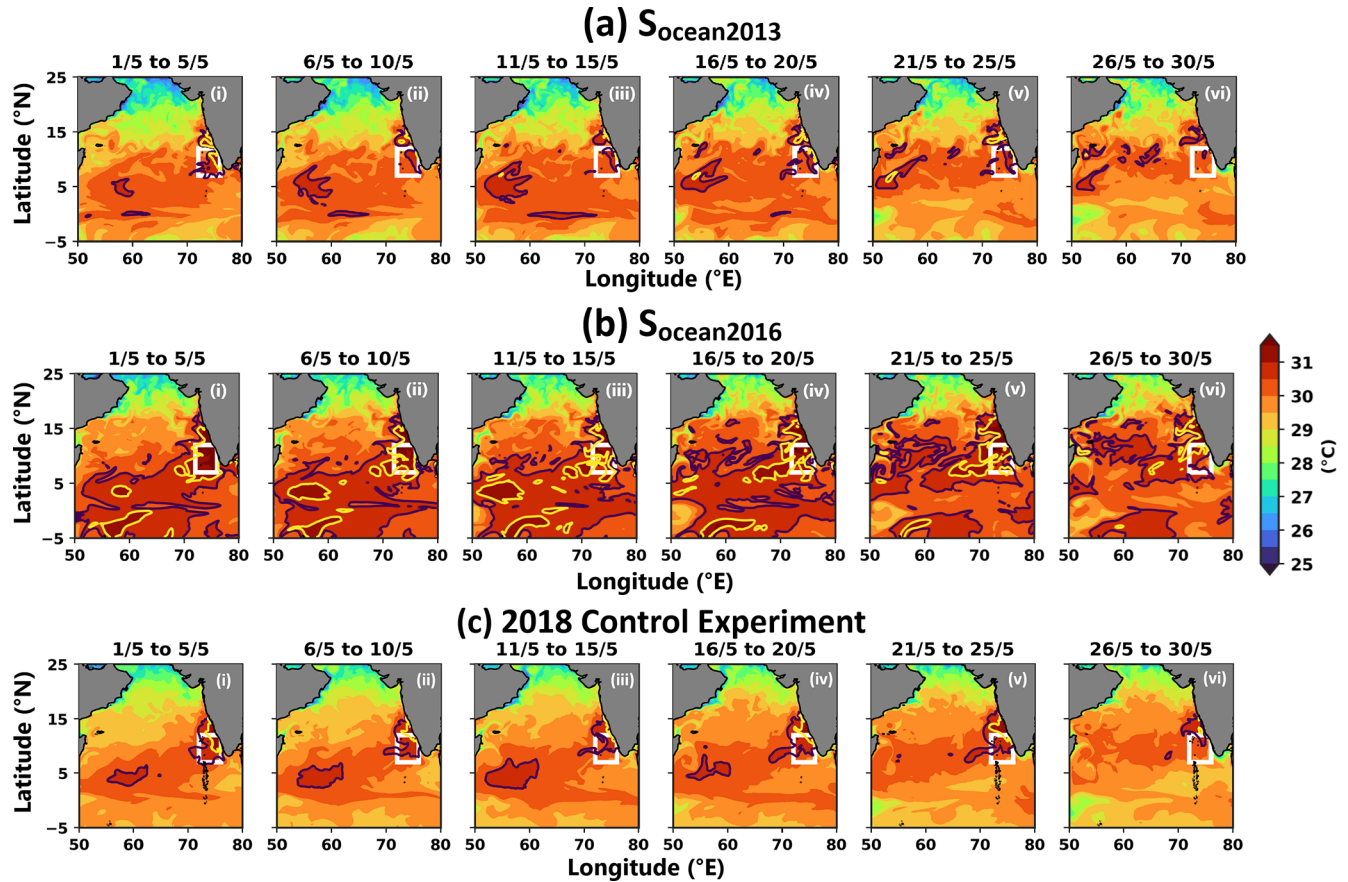


Figure 9. The 5 d average evolution of SST from 1 to 30 May for the (a) $S_{ocean2013}$, (b) $S_{ocean2016}$, and (c) 2018 control experiments. In the $S_{ocean2013}$ and $S_{ocean2016}$ experiments, the ocean’s initial condition was replaced to 2013 and 2016 in the 2018 control experiment. See Table 1 for further details about the experiments. The black and yellow contours represent 30.5 and 31 $^{\circ}\text{C}$, respectively. The days associated with mean evolution are displayed at the top of each panel. The white box is the core MWP region.

shadow zone was developed in the SEAS from 17 to 20 May, resulting in the largest MWP expansion in 2018 control, $S_{ocean2013}$, and $S_{ocean2016}$ experiments. Once the southwesterly wind strengthened, the P_{TKE} increased, and the ocean lost heat at the surface (Figs. 13a and 14a). In the 2013 control and $S_{atmos2013}$ experiments, atmospheric conditions were identical, and the ocean gained heat (Fig. S11b). The wind-induced P_{TKE} was higher in SEAS, and no such wind shadow zone was developed (Fig. 14b). Subsequently, the MWP was absent in these two experiments. In the 2016 control and $S_{atmos2016}$ experiments, the wind shadow zone was expanded over a comparatively large area from 1 to 8 May (Fig. 14c). Besides, the ocean received heat during this time in SEAS, creating favorable conditions for the development of the strong MWP (Fig. S11c).

4 Conclusion

A coupled atmosphere–ocean numerical model has been employed to investigate the formation and evolution of the

MWP in the SEAS. The model is simulated for three independent years: 2013, 2016, and 2018. The simulated results can reproduce the MWP features and showed good agreement with satellite and buoy data (Figs. 2–5 and S2–S5). The evolution of the atmospheric and ocean features near the SEAS from the mature to the dissipation day is well represented in the model. Four sensitivity experiments further elucidated the roles of oceanic and atmospheric conditions in the MWP formation. The changes in ocean initial conditions substantially impacted the magnitude of the MWP core temperature, resulting in 0.6 $^{\circ}\text{C}$ higher temperature in $S_{ocean2016}$ and 0.3 $^{\circ}\text{C}$ lower temperature in $S_{ocean2013}$ compared to the 2018 control experiment (Fig. S10d and e are compared with Fig. S10a), indicating the influence of the ocean initial condition in the MWP intensity. Analysis of the mixed-layer heat budget (Fig. 11) revealed that net surface heat flux is the primary driver of the MWP development, contributing significantly to the increase in mixed-layer temperature in the control and sensitivity experiments. It contributed more than 0.1 $^{\circ}\text{C d}^{-1}$ to the increased temperature just before the MWP matured on the day of 2018. Verti-

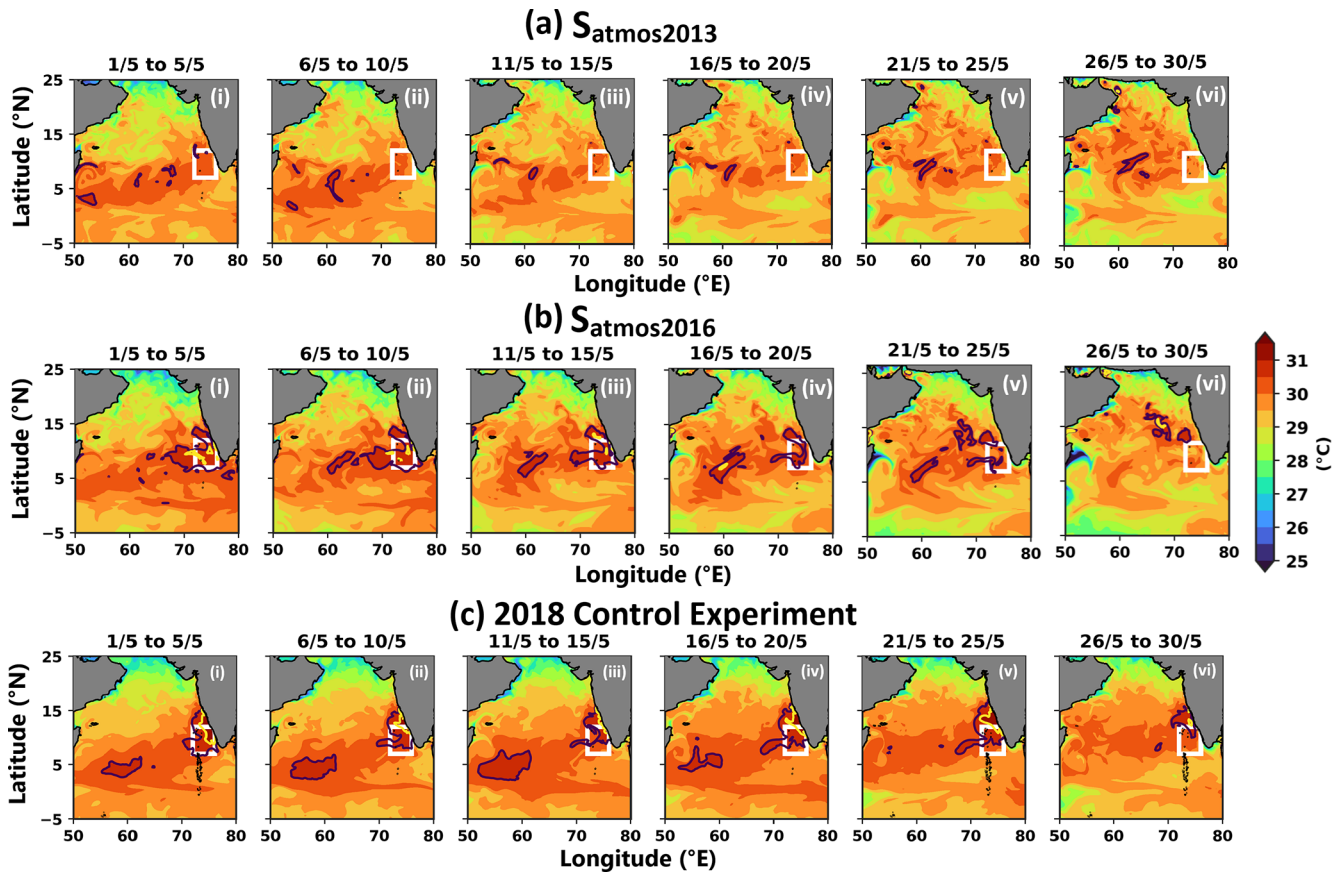


Figure 10. The 5 d average evolution of SST from 1 to 30 May for the experiment (a) $S_{\text{ocean2013}}$, (b) $S_{\text{ocean2016}}$, and (c) 2018 control experiments. In the $S_{\text{ocean2013}}$ and $S_{\text{ocean2016}}$ experiments, the atmospheric condition was replaced in 2013 and 2016 in the 2018 control experiment. See Table 1 for further details about the experiments. The black and yellow contours represent 30.5 and 31 °C, respectively. The days associated with mean evolution are displayed at the top of each panel. The white box is the core MWP region.

cal processes negatively affected temperature tendencies and could reach as high as -0.08 °C d^{-1} . As the moisture-rich southwesterly wind strengthened in late May to early June, it caused cloudiness, blocking the incoming shortwave radiation and the loss of latent heat flux in the SEAS (Figs. S6 and S8). Thus, the net surface heat flux, along with vertical processes, emerges as the primary driver behind the dissipation of the MWP (Fig. 11).

The atmospheric conditions remain the same in the 2018 control experiment, $S_{\text{ocean2013}}$, and $S_{\text{ocean2016}}$ experiments. Since the wind governs the MWP's advancement from mature to dissipation day by primarily controlling the net surface heat flux and the vertical processes, we have observed an identical contribution of the net surface heat flux and the vertical processes on the temperature tendency in these three experiments (Fig. 11a, d, and e). The MWP did not emerge in 2013, and when we replaced the atmospheric (ocean) condition of the 2018 control experiment with the 2013 control experiment in the $S_{\text{atmos2013}}$ ($S_{\text{ocean2013}}$) sensitivity experiment, we saw an 82 % reduction (8.5 % reduction) in MWP intensity index when compared to the

2018 control experiment. This suggested that in the weak-MWP year, although the ocean preconditions were met, the atmospheric forcing restricted the development of the MWP in SEAS. The MWP intensity index also revealed that the shuffling of the atmospheric forcings and oceanic initial conditions of the strong-MWP year to the year of the MWP whose intensity was identical to climatology ($S_{\text{atmos2016}}$ and $S_{\text{ocean2016}}$ experiments) resulted in a substantial decrease of 41 % and increase of 136 % in the MWP intensity index (Fig. 12), which demonstrated that in the strong-MWP year, the pre-April ocean condition played a considerable role in the development of the MWP in May, which was further supported by the prevailing atmospheric conditions.

Later, P_{TKE} was computed to study the mixing in the SEAS. The influence of wind-induced P_{TKE} on mixing surpassed that of P_{TKE} caused by thermal and haline buoyancy flux (Fig. 13). Further, a wind shadow zone with a lower P_{TKE} was witnessed in SEAS. The MWP advanced within this zone (Fig. 14). However, this shadow zone was absent in experiments such as the 2013 control and $S_{\text{atmos2013}}$ experiments. The MWP did not develop in these

Mixed Layer Heat Budget

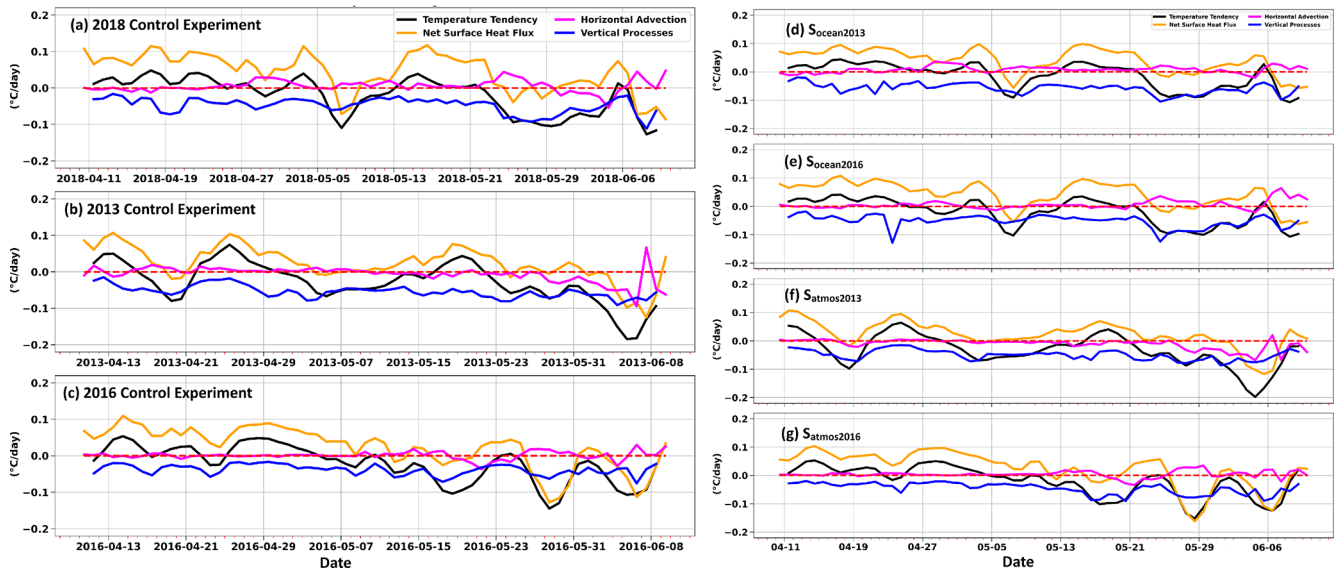


Figure 11. Area-averaged ($72\text{--}76^{\circ}\text{E}$ and $7\text{--}13^{\circ}\text{N}$, i.e. the white box shown in Fig. 1) mixed-layer heat budget for three control experiments – (a) 2018 control experiment, (b) 2013 control experiment, and (c) 2016 control experiment – and four sensitivity experiments – (d) $S_{\text{ocean}2013}$, (e) $S_{\text{ocean}2016}$, (f) $S_{\text{atmos}2013}$, and (g) $S_{\text{atmos}2016}$. In the sensitivity experiments, the oceanic and atmospheric conditions have been changed to various years; thus, only the day and month are kept on the x axis (d–g). For better understanding, the mixed-layer heat budget is shown from 10 April even though we consider 1 to 30 April the spin-up time.

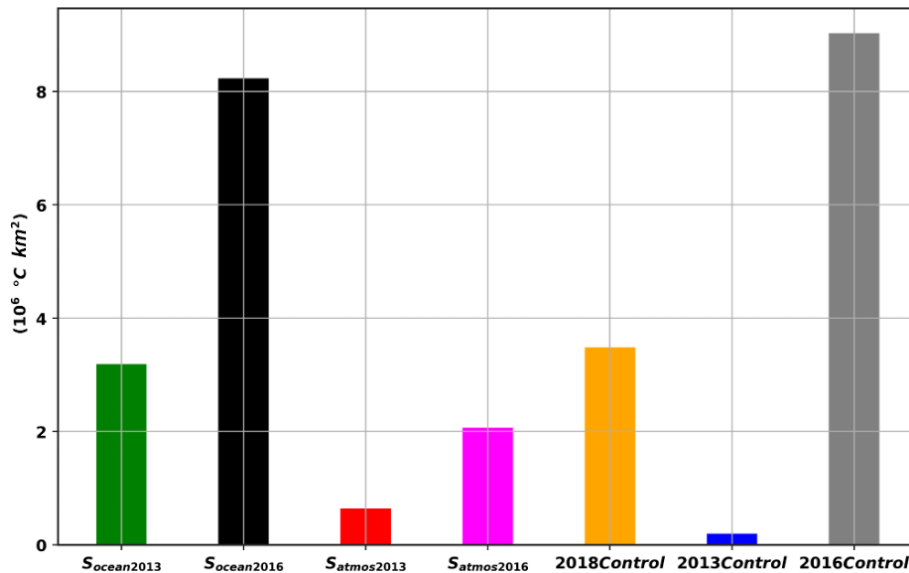


Figure 12. A comparison between the MWP intensity index in all three experiments during the respective mature-phase days in different years. In $S_{\text{ocean}2013}$, $S_{\text{ocean}2016}$, $S_{\text{atmos}2013}$, 2013 control experiment, and 2018 control experiment, the mature day was 20 May. In the $S_{\text{atmos}2016}$ and 2016 control experiments, the mature day was 4 May.

two experiments, although the ocean preconditions were met, indicating that the wind shadow zone was a key factor in the MWP’s advancement within the SEAS.

In conclusion, once the ocean conditions before April have laid the foundation (1 in Fig. 15), the prevailing atmospheric

conditions develop a weak wind zone in SEAS in May (2 in Fig. 15), and the incoming shortwave radiation flux under the clear sky is trapped within this zone (3 in Fig. 15). Subsequently, the MWP advances inside this area. Thus, a strong MWP can only occur in SEAS if all of these requirements are

Comparison of P_{TKE} by Wind Stirring, Thermal and Haline Buoyancy Flux in SEAS

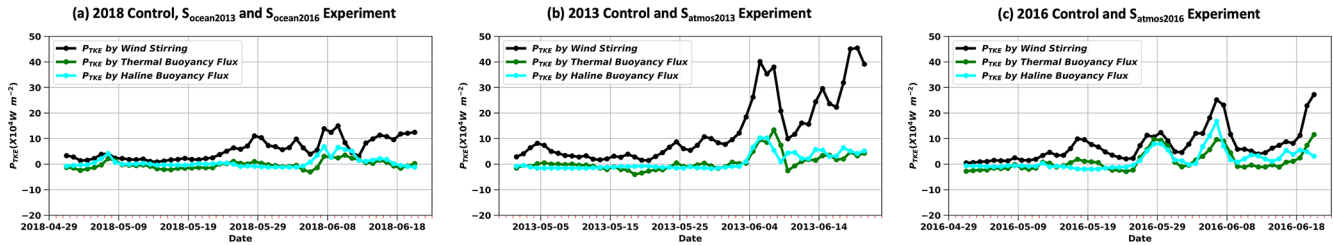


Figure 13. Comparison of the production of turbulent kinetic energy by wind, thermal, and haline buoyancy flux averaged in the SEAS (72–76° E and 7–13° N) from 1 May to 20 June. The values shown here are after multiplying by 10^4 .

P_{TKE} by Wind

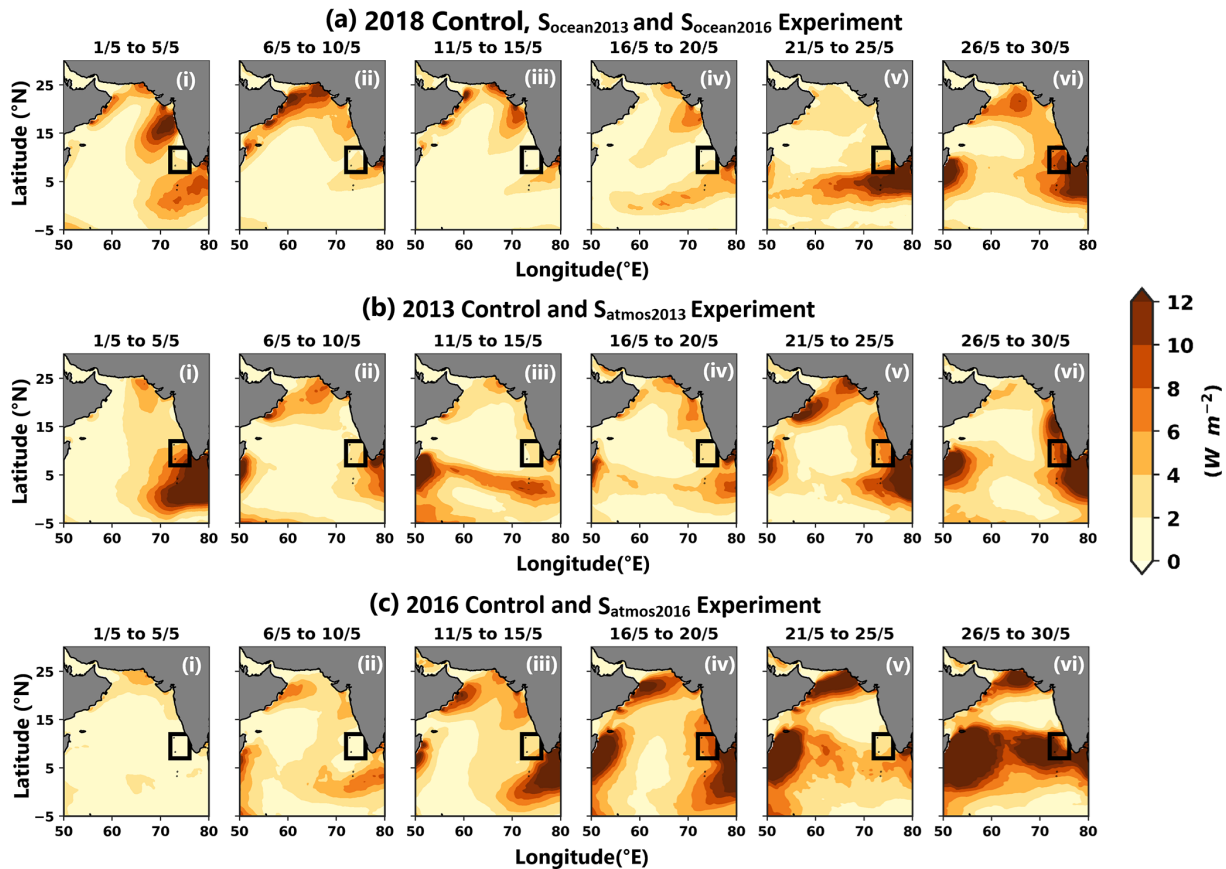


Figure 14. The 5 d average evolution of wind-induced production of turbulent kinetic energy for all control and sensitivity experiments. The fill values are shown after multiplying 10^4 . Atmospheric forcings are identical for the 2018 control, $S_{ocean2013}$, and $S_{ocean2016}$ experiments. Likewise, the wind-induced production of turbulent kinetic energy remains the same across all three experiments (a). Similarly, the wind-induced production of turbulent kinetic energy owing to thermal buoyancy flux in the 2013 control experiment and $S_{ocean2013}$ (b) and the 2016 control experiment and $S_{ocean2016}$ (c) are identical. Table 1 shows details from the sensitivity experiments. The days associated with mean evolution are listed at the top of each panel.

met (Fig. 15). After the MWP matures, the strong southwesterly wind in SEAS creates cloudiness and increases P_{TKE} , which blocks incoming shortwave radiation and causes the MWP to dissipate as the net surface heat flux decreases. The current study seeks to understand the impact of the ocean

and atmosphere on the MWP during its mature phase and the factors that contribute to its dissipation. We concluded that atmospheric conditions such as wind influence the spatial variability in the MWP. Nonetheless, ocean preconditions before April have a substantial effect on MWP strength. Given

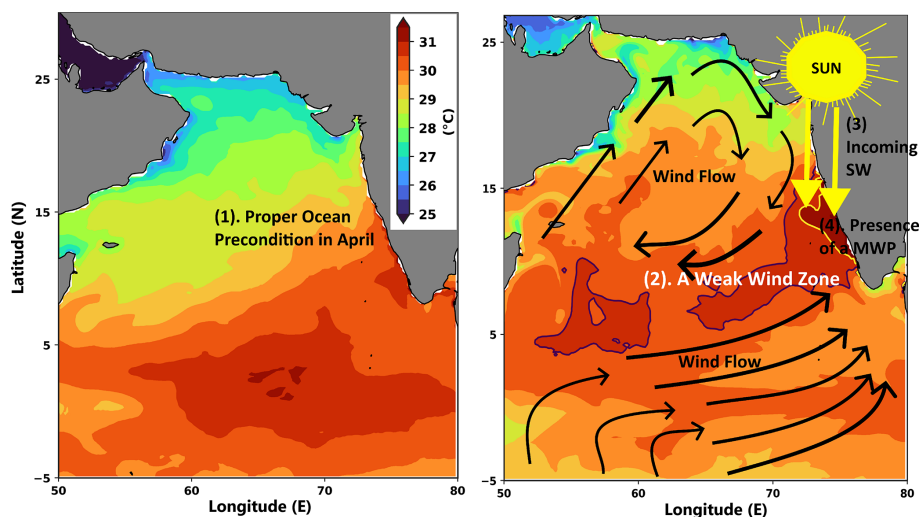


Figure 15. Schematic of the atmospheric and oceanic conditions associated with the formation of the MWP. The numbering denotes the importance of that process in the formation of the MWP. For instance, the ocean precondition (1) is the first requirement for MWP's genesis. Later, a weak wind zone (2) with less mixing traps the incoming shortwave radiation (3) in SEAS, which results in the formation of the MWP (4). Both panels have the same color bar levels. The black and yellow contours represent 30.5 and 31 °C, respectively.

the importance of ocean preconditioning in MWP genesis, it would be interesting to analyze the warming chronology of the southeastern Arabian Sea before the formation of a strong MWP, such as in 2016, which serves as the future scope of the current study. Besides, the wind shadow zone appears during a year with high MWP SST, and we hypothesize that this shadow zone and the resulting increase in MWP SST is linked with the onset of the Indian summer monsoon. However, further investigation is necessary, which is beyond the scope of the present study.

Code availability. Authors gratefully acknowledge USGS for making the COAWST numerical model available openly. In this study, Python is used for the graphical plots. In addition, the Gibbs Seawater package (McDougall and Barker, 2011) (<https://www.teos-10.org/software.htm#1>, last access: 18 February 2025) is utilized to compute basic oceanic parameters. Further, wrf-python is used to handle the WRF output (<https://doi.org/10.5065/D6W094P1>, Ludwig, 2019). Software/programs related to the study may be available from the corresponding author upon request.

Data availability. SODA3.4.2 data are used to give initial and boundary conditions to the ocean part of the numerical model (Carton et al., 2018), whereas ERA5 data are used for the atmospheric boundary and initial conditions (Hersbach et al., 2020). NOAA-AVHRR SST data are downloaded from <https://doi.org/10.7289/v52j68xx> (Saha et al., 2018). OSCAR current data are used to validate the model (Bonjean and Lagerloef, 2002). The AD10 moored buoy data can be requested from the Indian National Centre for Ocean Information Services (INCOIS) website (<https://incois.gov.in/portal/datainfo/drform.jsp>, IN-

COIS, 2023). All the model output data used in this study are available upon request.

Supplement. The supplement related to this article is available online at <https://doi.org/10.5194/os-21-1271-2025-supplement>.

Author contributions. SPL ran the numerical models, analyzed the results, and wrote the first draft of the manuscript. KRP helped in analysis and manuscript editing. VP reviewed the manuscript and supervised the work. All the authors agreed to the final version of the manuscript.

Competing interests. The contact author has declared that none of the authors has any competing interests.

Disclaimer. Publisher's note: Copernicus Publications remains neutral with regard to jurisdictional claims made in the text, published maps, institutional affiliations, or any other geographical representation in this paper. While Copernicus Publications makes every effort to include appropriate place names, the final responsibility lies with the authors.

Acknowledgements. This work is a part of Sankar Prasad Lahiri's doctoral thesis work. Sankar Prasad Lahiri is grateful to the Ministry of Education, Government of India, for the awarding of the Prime Minister's Research Fellowship (ref. no. IITD/Admission/Ph.D./PMRF/2020-21/380299) to pursue his doctoral research work at IIT-Delhi, India. The computational resources acquired through the high-performance computing (HPC)

cluster at IIT-Delhi are acknowledged. We thank the two anonymous reviewers for their insightful comments.

Financial support. Sankar Prasad Lahiri has been supported by the Ministry of Education, Government of India, through the awarding of the Prime Minister's Research Fellowship (ref. no. IITD/Admission/Ph.D./PMRF/2020-21/380299).

Review statement. This paper was edited by Aida Alvera-Azcárate and reviewed by two anonymous referees.

References

- Abram, N. J., Gagan, M. K., McCulloch, M. T., Chappell, J., and Hantoro, W. S.: Coral reef death during the 1997 Indian Ocean Dipole linked to Indonesian wildfires, *Science*, 301, 952–955, <https://doi.org/10.1126/science.1083841>, 2003.
- Akhil, V. P., Lengaigne, M., Krishnamohan, K. S., Keerthi, M. G., and Vialard, J.: Southeastern Arabian Sea Salinity variability: mechanisms and influence on surface temperature, *Clim. Dynam.*, 61, 3737–3754, <https://doi.org/10.1007/s00382-023-06765-z>, 2023.
- Arakawa, A. and Lamb, V. R.: Computational design of the basic dynamical process of the UCLA general circulation model, *Meth. Comp. Phys.*, 17, 173–265, 1977.
- Banzon, V., Smith, T. M., Mike Chin, T., Liu, C., and Hankins, W.: A long-term record of blended satellite and in situ sea-surface temperature for climate monitoring, modeling and environmental studies, *Earth Syst. Sci. Data*, 8, 165–176, <https://doi.org/10.5194/essd-8-165-2016>, 2016.
- Bonjean, F. and Lagerloef, G. S. E.: Diagnostic model and analysis of the surface currents in the Tropical Pacific Ocean, *J. Phys. Oceanogr.*, 32, 2938–2954, [https://doi.org/10.1175/1520-0485\(2002\)032<2938:DMAAOT>2.0.CO;2](https://doi.org/10.1175/1520-0485(2002)032<2938:DMAAOT>2.0.CO;2), 2002.
- Boutin, J., Reul, N., Koehler, J., Martin, A., Catany, R., Guimbard, S., Rouffi, F., Vergely, J. L., Arias, M., Chakroun, M., Corato, G., Estella-Perez, V., Hasson, A., Josey, S., Khvorostyanov, D., Kolodziejczyk, N., Mignot, J., Olivier, L., Reverdin, G., Stammer, D., Supply, A., Thouvenin-Masson, C., Turiel, A., Vialard, J., Cipollini, P., Donlon, C., Sabia, R., and Mecklenburg, S.: Satellite-based sea surface salinity designed for ocean and climate studies, *J. Geophys. Res.-Oceans*, 126, e2021JC017676, <https://doi.org/10.1029/2021JC017676>, 2021.
- Bruce, J. G., Johnson, D. R., and Kindle, J. C.: Evidence for eddy formation in the eastern Arabian Sea during the northeast monsoon, *J. Geophys. Res.*, 99, 7651–7664, <https://doi.org/10.1029/94JC00035>, 1994.
- Bruce, J. G., Kindle, J. C., Kantha, L. H., Kerling, J. L., and Bailey, J. F.: Recent observations and modeling in the Arabian Sea lac-cadive high region, *J. Geophys. Res.-Oceans*, 103, 7593–7600, <https://doi.org/10.1029/97jc03219>, 1998.
- Carniel, S., Benetazzo, A., Bonaldo, D., Falcieri, F. M., Miglietta, M. M., Ricchi, A., and Sclavo, M.: Scratching beneath the surface while coupling atmosphere, ocean and waves: Analysis of a dense water formation event. *Ocean Model.*, 101, 101–112, <https://doi.org/10.1016/j.ocemod.2016.03.007>, 2016.
- Carton, J. A., Chepurin, G. A., and Chen, L.: SODA3: A new ocean climate reanalysis, *J. Climate*, 31, 6967–6983, <https://doi.org/10.1175/jcli-d-18-0149.1>, 2018.
- Chakraborty, T., Pattnaik, S., Baisya, H., and Vishwakarma, V.: Investigation of Ocean Sub-Surface Processes in Tropical Cyclone Phailin Using a Coupled Modeling Framework: Sensitivity to Ocean Conditions, *Oceans*, 3, 364–388, <https://doi.org/10.3390/oceans3030025>, 2022.
- Chakraborty, T., Pattnaik, S., and Baisya, H.: Investigating the precipitation features of monsoon deep depressions over the Bay of Bengal using high-resolution stand-alone and coupled simulations, *Q. J. Roy. Meteorol. Soc.*, 149, 1213–1235, <https://doi.org/10.1002/qj.4449>, 2023.
- Dai, Q., Han, D., Rico-Ramirez, M. A., and Islam, T.: The impact of raindrop drift in a three-dimensional wind field on a radar-gauge rainfall comparison, *Int. J. Remote Sens.*, 34, 7739–7760, <https://doi.org/10.1080/01431161.2013.826838>, 2013.
- Deepa, R., Seetaramayya, P., Nagar, S. G., and Gnanaseelan, C.: On the plausible reasons for the formation of onset vortex in the presence of Arabian Sea mini warm pool, *Current Sci.*, 92, 794–800, 2007.
- Doval, M. D. and Hansell, D. A.: Organic carbon and apparent oxygen utilization in the western South Pacific and the central Indian Oceans, *Mar. Chem.*, 68, 249–264, [https://doi.org/10.1016/S0304-4203\(99\)00081-X](https://doi.org/10.1016/S0304-4203(99)00081-X), 2000.
- Dudhia, J.: Numerical study of convection observed during the Winter Monsoon Experiment using a mesoscale two-dimensional model, *J. Atmos. Sci.*, 46, 3077–3160, [https://doi.org/10.1175/1520-0469\(1989\)046<3077:NSOCOD>2.0.CO;2](https://doi.org/10.1175/1520-0469(1989)046<3077:NSOCOD>2.0.CO;2), 1989.
- Durand, F., Shetye, S. R., Vialard, J., Shankar, D., Shenoi, S. S. C., Ethe, C., and Madec, G.: Impact of temperature inversions on SST evolution in the Southeastern Arabian Sea during the pre-summer monsoon season, *Geophys. Res. Lett.*, 31, L01305, <https://doi.org/10.1029/2003GL018906>, 2004.
- Durand, F., Shankar, D., de Boyer Montégut, C., Shenoi, S. S. C., Blanke, B., and Madec, G.: Modeling the barrier-layer formation in the southeastern Arabian Sea, *J. Climate*, 20, 2109–2120, <https://doi.org/10.1175/JCLI4112.1>, 2007.
- Foltz, G. R. and McPhaden, M. J.: Impact of barrier layer thickness on SST in the central tropical North Atlantic, *J. Climate*, 22, 285–299, <https://doi.org/10.1175/2008JCLI2308.1>, 2009.
- Girishkumar, M. S., Joseph, J., Thangaprakash, V. P., Potapinjara, V., and McPhaden, M. J.: Mixed Layer Temperature Budget for the Northward Propagating Summer Monsoon Intraseasonal Oscillation (MISO) in the Central Bay of Bengal, *J. Geophys. Res.-Oceans*, 122, 8841–8854, <https://doi.org/10.1002/2017JC013073>, 2017.
- Gopalakrishna, V. V., Johnson, Z., Salgaonkar, G., Nisha, K., Rajan, C. K., and Rao, R. R.: Observed variability of sea surface salinity and thermal inversions in the Lakshadweep Sea during contrast monsoons, *Geophys. Res. Lett.*, 32, L18605, <https://doi.org/10.1029/2005GL023280>, 2005.
- Haidvogel, D. B., Arango, H. G., Hedstrom, K., Beckmann, A., Malanotte-Rizzoli, P., and Shchepetkin, A. F.: Model evaluation experiments in the North Atlantic Basin: Simulations in nonlinear terrain-following coordinates, *Dynam. Atmos. Oceans*, 32, 239–281, [https://doi.org/10.1016/S0377-0265\(00\)00049-X](https://doi.org/10.1016/S0377-0265(00)00049-X), 2000.

- Han, W., McCreary, J. P., and Kohler, K. E.: Influence of precipitation minus evaporation and Bay of Bengal rivers on dynamics, thermodynamics, and mixed layer physics in the upper Indian Ocean, *J. Geophys. Res.-Oceans*, 106, 6895–6916, <https://doi.org/10.1029/2000jc000403>, 2001.
- Hareesh Kumar, P. V., Sanilkumar, K. V., and Prasada Rao, C. V. K.: Arabian sea mini warm pool and its influence on acoustic propagation, *Defence Sci. J.*, 57, 115–121, <https://doi.org/10.14429/dsj.57.1738>, 2007.
- Hareesh Kumar, P. V., Joshi, M., Sanilkumar, K. V., Rao, A. D., Anand, P., Anil Kumar, K., and Prasada Rao, C. V. K.: Growth and decay of the Arabian Sea mini warm pool during May 2000: Observations and simulations, *Deep-Sea Res. Pt. I*, 56, 528–540, <https://doi.org/10.1016/j.dsr.2008.12.004>, 2009.
- Hastenrath, S. and Greischar, L. L.: Climatic atlas of the Indian Ocean. Part III: upper-ocean structure, *Geogr. J.*, 157, 216–216, <https://doi.org/10.2307/635289>, 1989.
- He, Q., Zhan, H., and Cai, S.: Anticyclonic Eddies Enhance the Winter Barrier Layer and Surface Cooling in the Bay of Bengal, *J. Geophys. Res.-Oceans*, 125, e2020JC016524, <https://doi.org/10.1029/2020JC016524>, 2020.
- Hersbach, H., Bell, B., Berrisford, P., Hirahara, S., Horányi, A., Muñoz-Sabater, J., Nicolas, J., Peubey, C., Radu, R., Schepers, D., Simmons, A., Soci, C., Abdalla, S., Abellan, X., Balsamo, G., Bechtold, P., Biavati, G., Bidlot, J., Bonavita, M., De Chiara, G., Dahlgren, P., Dee, D., Diamantakis, M., Dragani, R., Fleming, J., Forbes, R., Fuentes, M., Geer, A., Haimberger, L., Healy, S., Hogan, R. J., Hólm, E., Janisková, M., Keeley, S., Laloyaux, P., Lopez, P., Lupu, C., Radnoti, G., de Rosnay, P., Rozum, I., Vamborg, F., Villaume, S., and Thépaut, J.-N.: The ERA5 global reanalysis, *Q. J. Roy. Meteorol. Soc.*, 146, 1999–2049, <https://doi.org/10.1002/qj.3803>, 2020.
- Hong, S. Y., Noh, Y., and Dudhia, J.: A new vertical diffusion package with an explicit treatment of entrainment processes, *Mon. Weather Rev.*, 134, 2318–2341, <https://doi.org/10.1175/MWR3199.1>, 2006.
- INCOIS: Ocean Observation Network-Ocean Moored buoy Network for Northern Indian, OMNI buoy data [data set], <https://incois.gov.in/portal/datainfo/drform.jsp> (last access: 6 June 2024), 2023.
- Jacob, R., Larson, J., and Ong, E.: $M \times N$ communication and parallel interpolation in community climate system model version 3 using the model coupling toolkit, *Int. J. High Perform. Comput. Appl.*, 19, 293–307, <https://doi.org/10.1177/1094342005056116>, 2005.
- Joseph, P. V.: Warm pool over the Indian Ocean and monsoon onset, *Winter, Trop. Ocean Atmos. Newsl.*, 53, 1–5, 1990.
- Kara, A. B., Rochford, P. A., and Hurlburt, H. E.: An optimal definition for ocean mixed layer depth, *J. Geophys. Res.-Oceans*, 105, 16803–16821, <https://doi.org/10.1029/2000jc900072>, 2000.
- Kurian, J. and Vinayachandran, P. N.: Mechanisms of formation of the Arabian Sea mini warm pool in a high-resolution Ocean General Circulation Model, *J. Geophys. Res.-Oceans*, 112, C05009, <https://doi.org/10.1029/2006JC003631>, 2007.
- Ladwig, W.: wrf-python (version 1.3.0), UCAR/NCAR [code], <https://doi.org/10.5065/D6W094P1>, 2019.
- Large, W. G. and Pond, S.: Open ocean momentum flux measurements in moderate to strong winds, *J. Phys. Oceanogr.*, 11, 324–336, 1981.
- Large, W. G., McWilliams, J. C., and Doney, S. C.: Oceanic vertical mixing: A review and a model with a nonlocal boundary layer parameterization, *Rev. Geophys.*, 32, 363–403, <https://doi.org/10.1029/94RG01872>, 1994.
- Li, N., Zhu, X., Wang, H., Zhang, S., and Wang, X.: Intra-seasonal and interannual variability of sea temperature in the Arabian Sea Warm Pool, *Ocean Sci.*, 19, 1437–1451, <https://doi.org/10.5194/os-19-1437-2023>, 2023.
- Lim, K. S. S. and Hong, S. Y.: Development of an effective double-moment cloud microphysics scheme with prognostic cloud condensation nuclei (CCN) for weather and climate models, *Mon. Weather Rev.*, 138, 1587–1612, <https://doi.org/10.1175/2009MWR2968.1>, 2010.
- Lukas, R. and Lindstrom, E.: The mixed layer of the western equatorial Pacific Ocean, *J. Geophys. Res.-Oceans*, 96, 3343–3357, <https://doi.org/10.1029/90jc01951>, 1991.
- Masson, S., Luo, J. J., Madec, G., Vialard, J., Durand, F., Gualdi, S., Guilyardi, E., Behera, S., Delecluse, P., Navarra, A., and Yamagata, T.: Impact of barrier layer on winter-spring variability of the southeastern Arabian Sea, *Geophys. Res. Lett.*, 32, L07703, <https://doi.org/10.1029/2004GL021980>, 2005.
- Mathew, S., Natesan, U., Latha, G., and Venkatesan, R.: Dynamics behind warming of the southeastern Arabian Sea and its interruption based on in situ measurements, *Ocean Dynam.*, 68, 457–467, <https://doi.org/10.1007/s10236-018-1130-3>, 2018.
- McDougall, T. J. and Barker, P. M.: Getting started with TEOS-10 and the Gibbs Seawater (GSW) Oceanographic Toolbox, Tech. Rep., ISBN 978-0-646-55621-5, SCOR/IAPSO WG127, <http://www.teos-10.org> (last access: 14 February 2025), 2011.
- Mlawer, E. J., Taubman, S. J., Brown, P. D., Iacono, M. J., and Clough, S. A.: Radiative transfer for inhomogeneous atmospheres: RRTM, a validated correlated- k model for the longwave, *J. Geophys. Res.-Atmos.*, 102, 16663–16682, <https://doi.org/10.1029/97jd00237>, 1997.
- Murty, V. S. N., Krishna, S. M., Nagaraju, A., Somayajulu, Y. K., Babu, V. R., Sengupta, D., Sindu, P. R., Ravichandran, M., and Rajesh, G.: On the warm pool dynamics in the southeastern Arabian Sea during April–May 2005 based on the satellite remote sensing and ARGO float data, *Remote Sens. Mar. Environ.*, 6406, 282–293, <https://doi.org/10.1117/12.694254>, 2006.
- Neema, C. P., Hareeshkumar, P. V., and Babu, C. A.: Characteristics of Arabian Sea mini warm pool and Indian summer monsoon, *Clim. Dynam.*, 38, 2073–2087, <https://doi.org/10.1007/s00382-011-1166-2>, 2012.
- Nigam, T., Pant, V., and Prakash, K. R.: Impact of Indian ocean dipole on the coastal upwelling features off the southwest coast of India, *Ocean Dynam.*, 68, 663–676, <https://doi.org/10.1007/s10236-018-1152-x>, 2018.
- Nyadjro, E. S., Subrahmanyam, B., Murty, V. S. N., and Shriver, J. F.: The role of salinity on the dynamics of the Arabian Sea mini warm pool, *J. Geophys. Res.-Oceans*, 117, C09002, <https://doi.org/10.1029/2012JC007978>, 2012.
- Olabarrieta, M., Warner, J. C., and Kumar, N.: Wave-current interaction in Willapa Bay, *J. Geophys. Res.-Oceans*, 116, C12014, <https://doi.org/10.1029/2011JC007387>, 2011.
- Olabarrieta, M., Warner, J. C., Armstrong, B., Zambon, J. B., and He, R.: Ocean-atmosphere dynamics during Hurricane Ida and Nor'Ida: An application of the coupled ocean-atmosphere-wave-sediment transport (COAWST) modeling system, *Ocean Model.*

- 43, 112–137, <https://doi.org/10.1016/j.ocemod.2011.12.008>, 2012.
- Paul, N., Sukhatme, J., Gayen, B., and Sengupta, D.: Eddy-Freshwater Interaction Using Regional Ocean Modeling System in the Bay of Bengal, *J. Geophys. Res.-Oceans*, 128, e2022JC019439, <https://doi.org/10.1029/2022JC019439>, 2023.
- Paulson, C. A.: Mathematical representation of wind speed and temperature profiles in the unstable atmospheric surface layer, *J. Appl. Meteorol.*, 9, 857–861, 1970.
- Phillips, N. A.: a coordinate system having some special advantages for numerical forecasting, *J. Meteorol.*, 14, 184–185, [https://doi.org/10.1175/1520-0469\(1957\)014<0184:acshss>2.0.co;2](https://doi.org/10.1175/1520-0469(1957)014<0184:acshss>2.0.co;2), 1957.
- Prakash, K. R. and Pant, V.: Upper oceanic response to tropical cyclone Phailin in the Bay of Bengal using a coupled atmosphere–ocean model, *Ocean Dynam.*, 67, 51–64, <https://doi.org/10.1007/s10236-016-1020-5>, 2017.
- Prakash, K. R. and Pant, V.: On the wave-current interaction during the passage of a tropical cyclone in the Bay of Bengal, *Deep-Sea Res. Pt. II*, 172, 104658, <https://doi.org/10.1016/j.dsr2.2019.104658>, 2020.
- Prakash, K. R., Nigam, T., and Pant, V.: Estimation of oceanic subsurface mixing under a severe cyclonic storm using a coupled atmosphere–ocean-wave model, *Ocean Sci.*, 14, 259–272, <https://doi.org/10.5194/os-14-259-2018>, 2018.
- Rao, R. R. and Sivakumar, R.: On the possible mechanisms of the evolution of a mini-warm pool during the pre-summer monsoon season and the genesis of onset vortex in the South-Eastern Arabian Sea, *Q. J. Roy. Meteorol. Soc.*, 125, 787–809, <https://doi.org/10.1002/qj.49712555503>, 1999.
- Rao, S. A., Gopalakrishna, V. V., Shetye, S. R., and Yamagata, T.: Why were cool SST anomalies absent in the Bay of Bengal during the 1997 Indian Ocean Dipole Event, *Geophys. Res. Lett.*, 29, 1555, <https://doi.org/10.1029/2001GL014645>, 2002.
- Ricchi, A., Miglietta, M. M., Falco, P. P., Benetazzo, A., Bonaldo, D., Bergamasco, A., Sclavo, M., and Carniel, S.: On the use of a coupled ocean-atmosphere-wave model during an extreme cold air outbreak over the Adriatic Sea, *Atmos. Res.*, 172, 48–65, <https://doi.org/10.1016/j.atmosres.2015.12.023>, 2016.
- Saha, K., Zhao, X., Zhang, H.-M., Casey, K. S., Zhang, D., Baker-Yeboah, S., Kilpatrick, K. A., Evans, R. H., Ryan, T., and Relf, J. M.: AVHRR Pathfinder version 5.3 level 3 collated (L3C) global 4 km sea surface temperature for 1981–Present, NOAA National Centers for Environmental Information [data set], <https://doi.org/10.7289/v52j68xx>, 2018 (additional data available at: <http://www.ncei.noaa.gov/data/sea-surface-temperature-optimuminterpolation/v2.1/access/avhrr/>, last access: 13 March 2024).
- Sandeep, K. K., Pant, V., Girishkumar, M. S., and Rao, A. D.: Impact of riverine freshwater forcing on the sea surface salinity simulations in the Indian Ocean, *J. Mar. Syst.*, 185, 40–58, <https://doi.org/10.1016/j.jmarsys.2018.05.002>, 2018.
- Sarma, V. V. S. S.: The influence of Indian Ocean Dipole (IOD) on biogeochemistry of carbon in the Arabian Sea during 1997–1998, *J. Earth Syst. Sci.*, 115, 433–450, <https://doi.org/10.1007/BF02702872>, 2006.
- Schott, F. A. and McCreary, J. P.: The monsoon circulation of the Indian Ocean, *Prog. Oceanogr.*, 51, 1–123, [https://doi.org/10.1016/S0079-6611\(01\)00083-0](https://doi.org/10.1016/S0079-6611(01)00083-0), 2001.
- Schott, F. A., Xie, S.-P., and McCreary Jr., J. P.: Indian Ocean circulation and climate variability, *Rev. Geophys.*, 47, RG1002, <https://doi.org/10.1029/2007RG000245>, 2009.
- Seelanki, V., Nigam, T., and Pant, V.: Upper-ocean physical and biological features associated with Hudhud cyclone: A bio-physical modelling study, *J. Mar. Syst.*, 215, 103499, <https://doi.org/10.1016/j.jmarsys.2020.103499>, 2021.
- Seetaramayya, P. and Master, A.: Observed air–sea interface conditions and a monsoon depression during MONEX-79, *Arch. Meteorol. Geophys. Bioclimatol. Ser. A*, 33, 61–67, <https://doi.org/10.1007/BF02265431>, 1984.
- Shankar, D. and Shetye, S. R.: On the dynamics of the Lakshadweep high and low in the southeastern Arabian Sea, *J. Geophys. Res.-Oceans*, 102, 12551–12562, <https://doi.org/10.1029/97JC00465>, 1997.
- Shankar, D., Vinayachandran, P. N., and Unnikrishnan, A. S.: The monsoon currents in the north Indian Ocean, *Prog. Oceanogr.*, 52, 63–120, [https://doi.org/10.1016/S0079-6611\(02\)00024-1](https://doi.org/10.1016/S0079-6611(02)00024-1), 2002.
- Shankar, D., Remya, R., Vinayachandran, P. N., Chatterjee, A., and Behera, A.: Inhibition of mixed-layer deepening during winter in the northeastern Arabian Sea by the West India Coastal Current, *Clim. Dynam.*, 47, 1049–1072, <https://doi.org/10.1007/s00382-015-2888-3>, 2016.
- Shee, A., Sil, S., Gangopadhyay, A., Gawarkiewicz, G., and Ravichandran, M.: Seasonal Evolution of Oceanic Upper Layer Processes in the Northern Bay of Bengal Following a Single Argo Float, *Geophys. Res. Lett.*, 46, 5369–5377, <https://doi.org/10.1029/2019GL082078>, 2019.
- Shenoi, S. S. C., Shankar, D., and Shetye, S. R.: On the sea surface temperature high in the Lakshadweep Sea before the onset of the southwest monsoon, *J. Geophys. Res.-Oceans*, 104, 15703–15712, <https://doi.org/10.1029/1998jc900080>, 1999.
- Skamarock, W. C. and Klemp, J. B.: A time-split nonhydrostatic atmospheric model for weather research and forecasting applications, *J. Comput. Phys.*, 227, 3465–3485, <https://doi.org/10.1016/j.jcp.2007.01.037>, 2008.
- Skamarock, W., Klemp, J., Dudhia, J., Gill, D. O., Barker, D., Duda, M. G., Huang, X.-Y., Wang, W., and Powers, J. G.: A Description of the Advanced Research WRF Version 3, University Corporation for Atmospheric Research [data set], <https://doi.org/10.5065/D68S4MVH>, 2008.
- Song, Y. and Haidvogel, D.: A semi-implicit ocean circulation model using a generalized topography-following coordinate system, *J. Comput. Phys.*, 115, 228–244, <https://doi.org/10.1006/jcph.1994.1189>, 1994.
- Sprattall, J. and Tomczak, M.: Evidence of the barrier layer in the surface layer of the tropics, *J. Geophys. Res.-Oceans*, 97, 7305–7316, <https://doi.org/10.1029/92jc00407>, 1992.
- Stevenson, J. W. and Niiler, P. P.: Upper Ocean Heat Budget During the Hawaii-to-Tahiti Shuttle Experiment, *J. Phys. Oceanogr.*, 13, 1894–1907, [https://doi.org/10.1175/1520-0485\(1983\)013<1894:uohbdt>2.0.co;2](https://doi.org/10.1175/1520-0485(1983)013<1894:uohbdt>2.0.co;2), 1983.
- Tewari, M., Chen, F., Wang, W., Dudhia, J., LeMone, M. A., Mitchell, K., Ek, M., Gayno, G., Wegiel, J., and Cuenca, R. H.: Implementation and verification of the unified Noah land surface model in the WRF model, 20th Conference on Weather Analysis and Forecasting/16th Conference on Numerical Weather Predic-

- tion, 14 January 2004, Seattle, WA, USA, American Meteorological Society, Seattle, WA, 2004.
- Umlauf, L. and Burchard, H.: A generic length-scale equation for geophysical turbulence models, *J. Mar. Res.*, 61, 235–265, <https://doi.org/10.1357/002224003322005087>, 2003.
- Vialard, J., Foltz, G. R., McPhaden, M. J., Duvel, J. P., and de Boyer Montégut, C.: Strong Indian Ocean sea surface temperature signals associated with the Madden-Julian Oscillation in late 2007 and early 2008, *Geophys. Res. Lett.*, 35, L19608, <https://doi.org/10.1029/2008GL035238>, 2008.
- Warner, J. C., Armstrong, B., He, R., and Zambon, J. B.: Development of a Coupled Ocean-Atmosphere-Wave-Sediment Transport (COAWST) Modeling System, *Ocean Model.*, 35, 230–244, <https://doi.org/10.1016/j.ocemod.2010.07.010>, 2010.
- Zambon, J. B., He, R., and Warner, J. C.: Investigation of hurricane Ivan using the coupled ocean–atmosphere–wave–sediment transport (COAWST) model, *Ocean Dynam.*, 64, 1535–1554, <https://doi.org/10.1007/s10236-014-0777-7>, 2014.
- Zhang, C. and Wang, Y.: Projected future changes of tropical cyclone activity over the Western North and South Pacific in a 20-km-Mesh regional climate model, *J. Climate*, 30, 5923–5941, <https://doi.org/10.1175/JCLI-D-16-0597.1>, 2017.